frontiers in Chemistry

REVIEW
published: 15 April 2021
doi: 10.3389/fchem.2021.637501

# Recent Advances in $TiO_2$-Based Heterojunctions for Photocatalytic $CO_2$ Reduction With Water Oxidation: A Review

*Kai Li*[1,2], *Chao Teng*[1]*, *Shuang Wang*[1,3] *and Qianhao Min*[2]*

[1]*Institute of Marine Biomedicine, Shenzhen Polytechnic, Shenzhen, China,* [2]*State Key Laboratory of Analytical Chemistry for Life Science, School of Chemistry and Chemical Engineering, Nanjing University, Nanjing, China,* [3]*College of Engineering and Applied Sciences, Nanjing University, Nanjing, China*

OPEN ACCESS

**Edited by:**
*Ping Yu,*
*Institute of Chemistry, China*

**Reviewed by:**
*Chang-Yong Nam,*
*Brookhaven National Laboratory, United States*
*Yuqing Lin,*
*Capital Normal University, China*
*Limin Zhang,*
*East China Normal University, China*

***Correspondence:**
*Chao Teng*
*tengchao@szpt.edu.cn*
*Qianhao Min*
*minqianhao@nju.edu.cn*

**Specialty section:**
*This article was submitted to Green and Sustainable Chemistry, a section of the journal Frontiers in Chemistry*

**Received:** *03 December 2020*
**Accepted:** *01 February 2021*
**Published:** *15 April 2021*

**Citation:**
*Li K, Teng C, Wang S and Min Q (2021) Recent Advances in $TiO_2$-Based Heterojunctions for Photocatalytic $CO_2$ Reduction With Water Oxidation: A Review. Front. Chem. 9:637501. doi: 10.3389/fchem.2021.637501*

Photocatalytic conversion of $CO_2$ into solar fuels has gained increasing attention due to its great potential for alleviating the energy and environmental crisis at the same time. The low-cost $TiO_2$ with suitable band structure and high resistibility to light corrosion has proven to be very promising for photoreduction of $CO_2$ using water as the source of electrons and protons. However, the narrow spectral response range (ultraviolet region only) as well as the rapid recombination of photo-induced electron-hole pairs within pristine $TiO_2$ results in the low utilization of solar energy and limited photocatalytic efficiency. Besides, its low selectivity toward photoreduction products of $CO_2$ should also be improved. Combination of $TiO_2$ with other photoelectric active materials, such as metal oxide/sulfide semiconductors, metal nanoparticles and carbon-based nanostructures, for the construction of well-defined heterostructures can enhance the quantum efficiency significantly by promoting visible light adsorption, facilitating charge transfer and suppressing the recombination of charge carriers, resulting in the enhanced photocatalytic performance of the composite photocatalytic system. In addition, the adsorption and activation of $CO_2$ on these heterojunctions are also promoted, therefore enhancing the turnover frequency (TOF) of $CO_2$ molecules, so as to the improved selectivity of photoreduction products. This review focus on the recent advances of photocatalytic $CO_2$ reduction via $TiO_2$-based heterojunctions with water oxidation. The rational design, fabrication, photocatalytic performance and $CO_2$ photoreduction mechanisms of typical $TiO_2$-based heterojunctions, including semiconductor-semiconductor (S-S), semiconductor-metal (S-M), semiconductor-carbon group (S-C) and multicomponent heterojunction are reviewed and discussed. Moreover, the $TiO_2$-based phase heterojunction and facet heterojunction are also summarized and analyzed. In the end, the current challenges and future prospects of the $TiO_2$-based heterostructures for photoreduction of $CO_2$ with high efficiency, even for practical application are discussed.

**Keywords: $TiO_2$-based photocatalysts, heterostructures, $CO_2$ photoreduction, water oxidation, high efficiency**

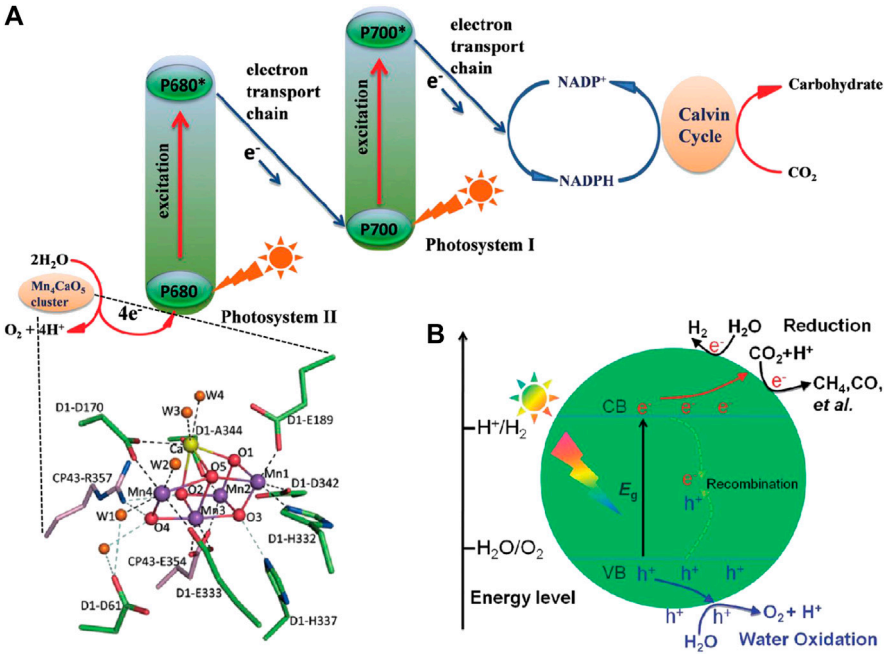


**FIGURE 1 |** Schematic diagrams of **(A)** natural photosynthesis and **(B)** semiconductor photocatalytic reduction of $CO_2$. Reproduced from Liu et al. (2016) with permission from Wiley-VCH and Wei et al. (2018) with permission from the Royal Society of Chemistry.

## INTRODUCTION

Energy and environmental crizes are two major bottlenecks restricting the sustainable development of human society. For a long time, the excessive consumption of fossil fuels has caused severe energy shortages, and the $CO_2$ released during the combustion process has become the main factor leading to global warming (Stott et al., 2000; Meinshausen et al., 2009; Solomon et al., 2009; Höök and Tang, 2013). It is urgent to develop and utilize renewable clean energy while reducing the concentration of $CO_2$ in the atmosphere (Brockway et al., 2019; Shindell and Smith, 2019). Notably, as a simple form of carbon storage, the rich carbon resources contained in $CO_2$ have huge development potential. Using $CO_2$ as a carbon feedstock to prepare carbon-based fuels can help alleviate the energy crisis and global warming at the same time, and has become a current research hotspot in the fields of both energy and environment (Olah et al., 2011; Kondratenko et al., 2013; Aresta et al., 2014; Ganesh, 2014; Li et al., 2019). However, the liner molecule with high thermodynamic stability and kinetic inertness makes it a great challenge for the activation and conversion of $CO_2$ (Ola and Maroto-Valer, 2015; Wei L. et al., 2018; Li et al., 2019; Nguyen et al., 2020). A lot of energy needs to be injected to break the C=O bond (dissociation energy about 750 kJ $mol^{-1}$) in $CO_2$ (Kim et al., 2017). Moreover, the extremely low water solubility of $CO_2$ (about 30 mM under 25°C at 1 atm) results in the low conversion efficiency of $CO_2$ in the aqueous reaction system (Xie et al., 2014). Therefore, a highly efficient reaction mode is also in great demand.

**TABLE 1 |** The possible reactions during the photocatalytic $CO_2$ reduction process.

| | Reactions | $\Delta G^0$ (kJ·$mol^{-1}$) |
|---|---|---|
| 1 | $H_2O\ (l) \rightarrow H_2\ (g) + 1/2O_2\ (g)$ | 237 |
| 2 | $CO_2\ (g) \rightarrow CO\ (g) + 1/2O_2\ (g)$ | 257 |
| 3 | $CO_2\ (g) + H_2O\ (l) \rightarrow HCOOH\ (l) + 1/2O_2\ (g)$ | 286 |
| 4 | $CO_2\ (g) + H_2O\ (l) \rightarrow HCHO\ (l) + O_2\ (g)$ | 522 |
| 5 | $CO_2\ (g) + 2H_2O\ (l) \rightarrow CH_3OH\ (l) + 3/2O_2\ (g)$ | 703 |
| 6 | $CO_2\ (g) + 2H_2O\ (l) \rightarrow CH_4\ (g) + 2O_2\ (g)$ | 818 |

Fortunately, the natural photosynthesis motivated by solar energy to covert $CO_2$ into carbonhydrates as well as the release of $O_2$ by water oxidation provides a very promising solution to reduce the $CO_2$ level in atmosphere, which inspires the development of artificial photosynthesis systems (Barber, 2009; Dogutan and Nocera, 2019; Zhang and Sun, 2019). As shown in **Figure 1A**, the water oxidation process takes place in the photosystem II (PSII) of green plants to provide electrons and protons for the $CO_2$ fixation and conversion in the photosystem I (PSI). Since a series of pioneering works devoted by Fujishima and Honda on semiconductor photocatalysis in the 1970s (Fujishima and Honda, 1972; Inoue et al., 1979), substantial efforts have been made for the combination of the two individual processes within a single artificial architecture to mimic the natural photosynthesis (shown in **Figure 1B**) during the past decades (Ma et al., 2014; Tu et al., 2014; White et al., 2015; Liu X. et al., 2016; Li et al., 2019; Xu and Carter, 2019).

**TABLE 2 |** Electrochemical potentials of $H_2O$ oxidation and $CO_2$ reduction into various products.

| | Reactions | $E^0$ (V) *vs.* NHE at pH 7 |
|---|---|---|
| 1 | $2H_2O + 4h^+ \rightarrow O_2 + 4H^+$ | 1.23 |
| 2 | $CO_2 + e^- \rightarrow CO_2^-$ | −1.9 |
| 3 | $CO_2 + 2H^+ + 2e^- \rightarrow CO + H_2O$ | −0.53 |
| 4 | $CO_2 + 2H^+ + 2e^- \rightarrow HCOOH$ | −0.61 |
| 5 | $CO_2 + 4H^+ + 4e^- \rightarrow HCHO + H_2O$ | −0.48 |
| 6 | $CO_2 + 6H^+ + 6e^- \rightarrow CH_3OH + H_2O$ | −0.38 |
| 7 | $CO_2 + 8H^+ + 8e^- \rightarrow CH_4 + 2H_2O$ | −0.24 |
| 8 | $2H^+ + 2e^- \rightarrow H_2$ | −0.41 |

In a typical semiconductor photocatalytic process, the semiconductor photocatalyst is excited by the incident photons with energy greater than or equal to its bandgap energy ($E_g$), where electrons ($e^-$) are excited to the conduction band (CB) to participate in the reduction reactions, remaining holes ($h^+$) in the valence band (VB) for the oxidation reactions. Considering that $CO_2$ molecule is very stable and the photocatalytic $CO_2$ reduction is a series of uphill reactions ($\Delta G^0>0$, see in **Table 1**) (Wei L. et al., 2018), a large energy input is necessary to covert $CO_2$ into solar fuels, corresponding to the photons in the ultraviolet or shortwave visible regions. In addition, the band structure of ideal semiconductors needs to meet the redox potentials of $CO_2$ reduction and water oxidation reactions at the same time, as listed in **Table 2** (Habisreutinger et al., 2013; White et al., 2015). Generally, the CB edge position ($E_{CB}$) should be more negative than the potential for reducing $CO_2$, whereas the VB edge position ($E_{VB}$) should be more positive than the potential for oxidizing $H_2O$ to $O_2$. So far, the photocatalytic activity of numerous photocatalysts, etc. $TiO_2$ (Habisreutinger et al., 2013; Ma et al., 2014; Ola and Maroto-Valer, 2015), ZnO (Lee K. M. et al., 2016; Nie et al., 2018; Kegel et al., 2018), $WO_3$ (Chen et al., 2012; Shi et al., 2019; Wang H. et al., 2019), $SnO_2$ (He et al., 2015; You et al., 2020), $Cu_2O$ (An et al., 2014; Shi et al., 2019), CdS (Kuai et al., 2015; Kuehnel et al., 2017; Wei Z. H. et al., 2018; Bie et al., 2019; Low et al., 2019), $Bi_2WO_6$ (Cao et al., 2018; Liu et al., 2021), $BiVO_4$ (Mao et al., 2012; Wei Z. H. et al., 2018), BiOBr (Ye et al., 2016; Wu et al., 2018), g-$C_3N_4$ (He et al., 2015; Nie et al., 2018; Thi Thanh Truc et al., 2019; Wang et al., 2020a) and graphene (An et al., 2014; Xiong et al., 2016; Shehzad et al., 2018a; Zhao H. et al., 2018; Bie et al., 2019), have been investigated intensively, in which few of them can realize the synergism of photocatalytic $CO_2$ reduction and water oxidation. In particular, the low-cost $TiO_2$ with suitable band structure and high resistibility to light corrosion is a very promising candidate, which has become the benchmark in this field (Habisreutinger et al., 2013; Ma et al., 2014; Ola and Maroto-Valer, 2015). However, the wide band gap of $TiO_2$ (3.2 eV for anatase) responses to UV light only, which accounts for only 3–5% of the incoming solar spectrum, thus restricting the conversion efficiency of solar energy. Besides, the fast recombination of photo-induced $e^-/h^+$ pairs within $TiO_2$ results in the low charge separation efficiency, therefore reducing its photocatalytic performance further. Moreover, the low selectivity toward photoreduction products of $CO_2$ based on aqueous $TiO_2$ suspension photocatalytic system should also be improved.

In the past few decades, various of strategies have been developed to enhance the photocatalytic performance of $TiO_2$. Among them, the nanostructured $TiO_2$ with single crystalline phase exhibited the decreased recombination rate of charge carriers, comparing to the polycrystalline samples that possess large amount of grain boundaries and defects acting as recombination centers (Tu et al., 2014; Xu et al., 2015). Moreover, crystal facet engineering has been adopted to tune the surface energy and active sites of $TiO_2$, contributing to the adsorption and activation of $CO_2$ (Liu L. et al., 2016; Xiong et al., 2018; Tu et al., 2020). Obviously, the preference adsorption of $CO_2$ molecules at the surface oxygen vacancy sites of $TiO_2$ can reduce the reactive barrier of $CO_2$ photoreduction reactions, in which one oxygen atom of $CO_2$ is trapped by a bridging oxygen vacancy defect to induce affinity interactions (Lee et al., 2011; Liu L. et al., 2016; Tan et al., 2017). Moreover, the localized electrons of oxygen vacancies can form adventitious energy levels, extending the photoresponsive range of semiconductor photocatalyst. Besides, surface oxygen vacancies with typical defect states can trap electrons or holes to inhibit their recombination (Wang et al., 2018). To sum up, the significance of surface oxygen vacancies on defected $TiO_2$ has been ascertained in the enhancement of $CO_2$ adsorption, activation, dissolution, and stabilization of reaction intermediates (Nguyen et al., 2020). In addition, metal/nonmetal ion doping is used to introduce additional energy level between the band gap of $TiO_2$, resulting in the reduced band width and enhanced visible light adsorption (Tu et al., 2014; Ola and Maroto-Valer, 2015; Shehzad et al., 2018b; Patil et al., 2019). Dye sensitized $TiO_2$ displays enhanced photoreduction efficiency of $CO_2$ due to the injection of photosensitized electrons from the energy level of dye molecule to the CB of $TiO_2$ with more negative potential, while the superior visible light responsibility of dye molecules can also improve the utilization of incident light (Ma et al., 2014; Ola and Maroto-Valer, 2015; Lee J. S. et al., 2016; Woo et al., 2019). Although these strategies have proven to be effective, the charge separation efficiency, light energy utilization and product selectivity still need to be further improved to fulfill the demand of more efficient photoreduction of $CO_2$, even for the practical application in the future.

As is known, construction of heterojunction between $TiO_2$ and cocatalyst with matching electronic band structures can significantly promote the separation of photogenerated $e^-$ and $h^+$, enlarge the spectra response range, while the physicochemical properties of some special cocatalyst can promote the photocatalytic $CO_2$ reduction or water oxidation to a certain extent, thereby resulting in high photoreduction efficiency of $CO_2$ over the heterostructured phocatalytic system with enhanced reduction products selectivity (Ma et al., 2014; Wang et al., 2014; Wei L. et al., 2018; Nguyen et al., 2020).

In addition to photocatalysts, photoreactors as well as reaction modes also play vital roles in affecting the photoreduction efficiency of $CO_2$. Generally, the two key parameters which determine the types of photoreactors

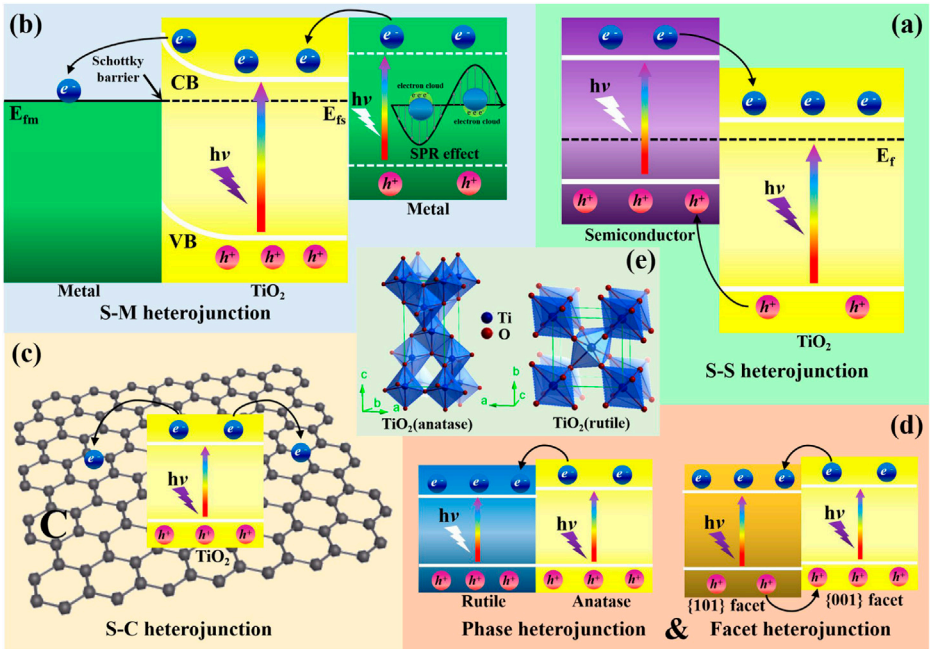


**FIGURE 2 |** Separation and transfer of photogenerated charge carriers in the $TiO_2$-based **(A)** S-S heterojunction, **(B)** S-M heterojunction, **(C)** S-C heterojunction and **(D)** phase and facet heterojunction; **(E)** Crystalline structures of $TiO_2$ (anatase) and $TiO_2$ (rutile).

utilized in $CO_2$ photoreduction are the phases involved (i.e., gas-solid, liquid-solid) and the mode of operation (i.e., batch, semi-batch or continuous). In the solid-liquid cases, photocatalysts are usually dispersed in alkaline mediums (aqueous solution) which can realize higher $CO_2$ solubility, resulting in the formation of $CO_3^{2-}$ and $HCO_3^-$. However, these species are difficult to be reduced in comparison with $CO_2$ (Corma and Garcia, 2013). In order to overcome the above drawbacks, the solid-vapor mode has been widely applied where the generation rate of the products for $CO_2$ photoreduction can be improved significantly (Xie et al., 2014; Xie et al., 2016; Xiong et al., 2017b). In addition, the exposure of photocatalysts in a $CO_2$ atmosphere can reduce the generation of $H_2$, thus enhancing the selectivity for $CO_2$ reduction. Obviously, the solid-vapor mode is more suitable for $CO_2$ photoreduction in the presence of $H_2O$.

In this review, we will mainly focus on the recent advances of photocatatytic $CO_2$ reduction processes with water oxidation using $TiO_2$-based heterojunction as photocatalysts. Different categories of heterojunctions, including S-S heterojunction (**Figure 2A**), S-M heterojunction (**Figure 2B**), S-C heterojunction (**Figure 2C**), multicomponent heterojunction, phase heterojunction and facet heterojunction (**Figure 2D**) are reviewed individually. In addition, the unique functions of cocatalysts among different heterostructured photocatalytic systems (etc. photosensitizer, $CO_2$ reduction promoter, water oxidation promoter and surface plasmon resonance (SPR) source) as well as the photoreduction mechanisms of $CO_2$ are discussed in detail. In the end, we will look forward to the prospects, opportunities and challenges of photocatalytic $CO_2$ reduction, predict the research directions of this field in the future, and put forward our opinions on the construction of efficient multifunctional integrated photocatalytic $CO_2$ reduction systems. We believe that this review will provide some useful guidelines for the construction of heterostructured photocatalysts for photoreduction of $CO_2$ with high performance in the future.

## PHOTOREDUCTION OF $CO_2$ TO SOLAR FUELS ON $TIO_2$-BASED HETEROJUNCTIONS

From the perspective of semiconductor photocatalysis, the premise of high photocatalytic efficiency is the efficient separation and rapid transfer of photogenerated $e^-/h^+$ pairs, thereby prolonging their lifetimes and inhibiting their recombination. The strategy for the construction of heterojunction by coupling semiconductor ($TiO_2$) with a secondary substance including other semiconductors (Aguirre et al., 2017; Yang et al., 2017; She et al., 2018; Xu et al., 2018a; Jin et al., 2019; Low et al., 2019; Thi Thanh Truc et al., 2019; Wu et al., 2019), metal nanoparticles (Xie et al., 2013; Neaţu et al., 2014; Jiao et al., 2015; Xiong et al., 2015; Lee K. Y. et al., 2016; Yu et al., 2016; Cheng et al., 2017; Tahir et al., 2017; Xiong et al., 2017C; Chong et al., 2018; Low et al., 2018; Tan et al., 2018; Tasbihi et al., 2018a; Wei Y. et al., 2018; Zhao Y. et al., 2018; Khatun et al., 2019; Wang R. et al., 2019; Zeng et al., 2020; Ziarati et al., 2020; Wang et al., 2021) and carbon-

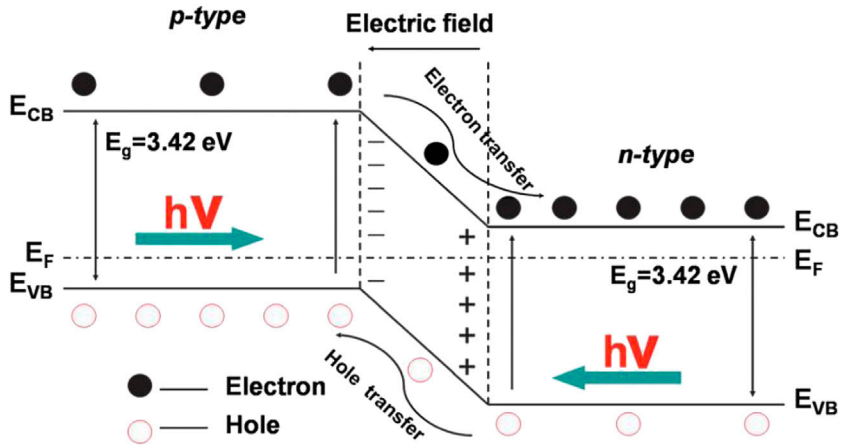


**FIGURE 3 |** Schematic diagram showing the energy band structure and electron-hole pair separation in the p-n heterojunction. Reproduced from Wang et al. (2014) with permission from the Royal Society of Chemistry.

based nanostructures (Xia et al., 2007; Tu et al., 2013; Gui et al., 2014; Chowdhury et al., 2015; Xiong et al., 2016; Lin et al., 2017; Tan et al., 2017; Wang et al., 2017; Li et al., 2018; Olowoyo et al., 2018; Shehzad et al., 2018a; Zhang J. et al., 2018; Zubair et al., 2018; Bie et al., 2019; Olowoyo et al., 2019; Wang R. et al., 2019; Rodríguez et al., 2020) has been generally applied. Since different phases (etc. anatase, brookite, or rutile) and exposed facets (etc. (001) or (101)) of $TiO_2$ exhibit various of band structure and reactivity, $TiO_2$-based phase heterojunction (Reñones et al., 2016; Hwang et al., 2019; Jin et al., 2019; Chen et al., 2020; Lee J. S. et al., 2016; Xiong et al., 2020) or facet heterojunction (Yu et al., 2014; Cao et al., 2016; Liu L. et al., 2016; Xiong et al., 2016; Xiong et al., 2017a; Di Liberto et al., 2019) are also fabricated for photocatalytic $CO_2$ reduction, which exhibits enhanced photocatalytic efficiency in comparison with pristine $TiO_2$. On the one hand, the heterostructure facilitates the separation of photoinduced charge carriers which then transfer across the heterointerface to restrain recombination. On the other hand, the additional active sites introduced by the cocatalysts favor for the adsorption and activation of $CO_2$, thus enhancing the photoreduction efficiency of $CO_2$. Besides, the promoted quantum efficiency and product selectivity can also be expected by the constructed heterojunctions, since light-excitation attributes, band structure, and separation efficiency of photogenerated charge carriers of heterojunctions play vital roles in the selectivity of $CO_2$ photoreduction products. Moreover, various cocatalysts with different reactive active sites can also affect the product selectivity greatly, where the adsorption/activation of $CO_2$ as well as the adsorption/desorption of the intermediates are tuned (Fu et al., 2019).

In this section, the rational design, fabrication, photocatalytic performance and photoreduction mechanism of $CO_2$ over the $TiO_2$-based typical categories of heterojunctions (S-S, S-M, S-C, multicomponent, phase and facet heterojunction) will be reviewed and discussed in detail. In addition, the selectivity toward photoreduction products is another focus. The relative mechanism was concluded and analyzed in the certain case.

## $TiO_2$ Based Z-scheme S-S Heterojunction for $CO_2$ Photoreduction

Coupling n-type $TiO_2$ with a p-type semiconductor possessing matching energy band structure to form a p-n heterojunction is one of the most classic S-S heterojunction (Zeng et al., 2014; Aguirre et al., 2017; Lee et al., 2017; Zhang L. et al., 2018; Iqbal et al., 2020; Zhang et al., 2020). As shown in **Figure 3**, the contacting of the two semiconductors leads to the diffusion of $e^-$ and $h^+$, then forms a space-charge region at the interface of the p-n heterojunction (Wang et al., 2014). As a result, a strong built-in electrical field is created which can drive the photoinduced $e^-$ and $h^+$ to transfer in the opposite directions, therefore enhancing the separation efficiency of charge carriers. In addition to p-n heterojunction, $TiO_2$-based non-p-n heterojunctions are also common (Yang et al., 2017; She et al., 2018; Jin et al., 2019; Low et al., 2019; Thi Thanh Truc et al., 2019; Wu et al., 2019). Typically, two closely integrated semiconductors with staggered band configurations can form a type II-1 heterojunction (shown in **Figure 4A**) (Zhang and Jaroniec, 2018), in which the band bending facilitates the charge transfer at the heterointerface. Specifically, $e^-$ and $h^+$ are separated individually in both semiconductor 1 (SC-1) and semiconductor 2 (SC-2) under the irradiation of incident light. The difference in energy level leads to the transfer of $e^-$ from the CB of SC-1 with more negative potential to the CB of SC-2. Meanwhile, $h^+$ can transfer from the VB of SC-2 to the VB of SC-1 with more positive potential. Similar to the p-n heterojunction, the reverse migration of $e^-$ and $h^+$ in the type II-1 heterojunction improves the separation efficiency of charge carriers, thus endowing the enhanced photocatalytic performance of the heterostructured system. However, the way of carrier transfer in the above

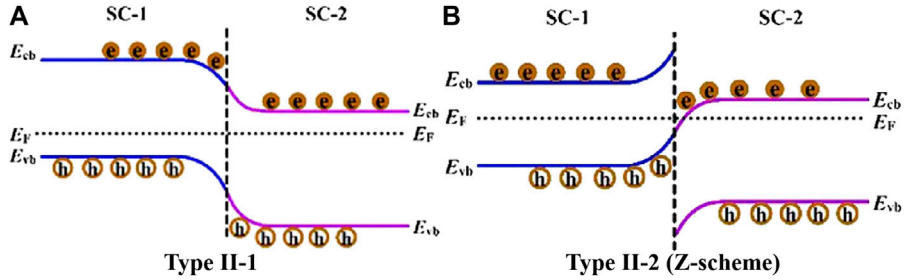


**FIGURE 4 |** Photogenerated charge carrier transfer process for two types of non p-n heterojunctions: **(A)** type II-1, and **(B)** type II-2 (direct Z-scheme). Reproduced from Zhang and Jaroniec (2018) with permission from Elsevier and Copyright Clearance Center.

heterojunctions will lead to a decrease in their redox ability, making it difficult to ensure the optimal photocatalytic activity.

Recently, study on the construction of all-solid-state Z-scheme heterojunction has gained great attention of researchers (Kuai et al., 2015; Aguirre et al., 2017; Takayama et al., 2017; Yang et al., 2017; She et al., 2018; Low et al., 2019; Thi Thanh Truc et al., 2019; Wang et al., 2019; Raza et al., 2020; Wang et al., 2020). Comparing to the p-n and type II-1 heterojunctions, the carrier transfer mode in the Z-scheme heterojunction is more favorable for photocatalytic application. In general, the band bending at the interface of direct Z-scheme heterojunction (type II-2) is conducive to the recombination of photoinduced $e^-$ and $h^+$ with weaker reduction and oxidation ability, so that $e^-$ in the more negative CB of SC-1 and $h^+$ in the more positive VB of SC-2 can be remained (shown in **Figure 4B**). As a result, both high separation efficiency and optimal redox ability of photoinduced charge carriers can be realized, thus endowing the high photocatalytic performance of the Z-scheme system. In this section, recent advances for the construction of $TiO_2$-based all-solid-state indirect and direct Z-scheme heterojunctions as well as their application for photocatalytic $CO_2$ reduction with water oxidation will be reviewed and discussed in detail. Photocatalytic $CO_2$ reduction performance of the typical $TiO_2$-based all-solid-state Z-scheme heterojunctions are listed in **Table 3**.

Construction of indirect Z-scheme system between $TiO_2$ and another semiconductor using noble metals such as Pt (Wang et al., 2020a), Au (Wang et al., 2020b) and Ag (Tahir, 2020) as electron mediators has gained increased attention due its enhanced separation efficiency of photogenerated $e^-/h^+$ pairs with the recombination of inefficient charge carriers, thereby improving the photoreduction efficiency of $CO_2$. As reported by Tahir, $ZnFe_2O_4$/Ag/$TiO_2$ nanocomposite was fabricated by physical mixing Ag/$TiO_2$ nanorods and $ZnFe_2O_4$ nanospheres in methanol solution under continuous stirring (Tahir, 2020). Compared to the point contact between 0D $TiO_2$ nanoarticles and 0D $ZnFe_2O_4$ nanospheres, the stronger interaction between 0D $ZnFe_2O_4$ nanospheres and 1D $TiO_2$ nanorods is beneficial to the transfer of photogenerated electrons and holes at the interface. At the same time, the migration of these charge carriers along the 1D nanostructure is more efficient, which significantly inhibits their recombination. Moreover, the UV irradiation induced Z-scheme carrier transfer pathway ensures the high redox capability of the remaining carriers with the recombination of inefficient species within Ag nanoparticles, resulting in the superior CO generation rate of 1025 μmol $g_{cat}^{-1}$ $h^{-1}$. Compared to $ZnFe_2O_4$, graphic-$C_3N_4$ (g-$C_3N_4$) is more preferred for the construction of $TiO_2$-based Z-scheme heterojunction due to its fully visible light utilization, improved $CO_2$ adsorption capacity (derived from its surface π bond) and proper band structure for $CO_2$ photoreduction with $H_2O$ oxidation (Wu et al., 2019; Wang et al., 2020a). Moreover, it can also trap photogenerated electrons to enhance charge separation efficiency within the heterojunction. On this basis, g-$C_3N_4$ was coated on the surface of Au/$TiO_2$ hybrid to form a Z-scheme photocatalyst (**Figure 5A,B**) for visible-light-driven (VLD) photocatalytic $CO_2$ reduction (Wang et al., 2020a). In particular, the efficient separation of photogenerated $e^-/h^+$ pairs within anatase $TiO_2$ is attributed to the formation of {001}/{101} facet heterojunction. Then, photogenerated electrons in the CB of $TiO_2$ are directionally transferred through Au and recombine with photogenerated holes in the VB of g-$C_3N_4$, thereby boosting the photoreduction of $CO_2$ by photogenerated electrons in the CB of g-$C_3N_4$ (shown in **Figure 5C**). Notably, the high selectivity toward $CO_2$ photoreduction (>99%) was realized with few $H_2$ generation, while the selectivity for $CH_4$ generation (63.3%) was also enhanced compared to pure g-$C_3N_4$ (1.4%). The following work of this group (Wang et al., 2020a) devoted to further improving the selectivity for $CH_4$ generation with high apparent quantum efficiency (AQE) under visible light irradiation, in which 3D ordered macroporous (3DOM) $TiO_2$@C was coupled with g-$C_3N_4$ using Pt as electron mediator (3DOM-CNPTC) (shown in **Figure 5D,E**). The DFT calculation revealed the enrichment of photogenerated electorns by abundant N-sites on the interface between Pt and g-$C_3N_4$, which can reduce the adsorbed $CO_2$ to $CH_4$ directly in the presence of $H_2O$, thereby improving the selectivity for $CH_4$ generation (81.7%). In addition, the strong visible light adsorption by g-$C_3N_4$ and Pt as well as the multiple scattering of incident light within the 3DOM structure (**Figure 5F**) result in the high AQE of the Z-scheme heterojunction (5.67%), which is 140 folds than that of P25 (0.04%). Interestingly, the interaction between $TiO_2$ and g-$C_3N_4$ could also be strengthened by Al-O links which was introduced into the Z-scheme through impregnation (Wu et al., 2019). Specifically, $TiO_2$ nanotubes (TNTs) fabricated *via* anodization of Ti foils are dipped

**TABLE 3 |** Photocatalytic $CO_2$ reduction performance on typical $TiO_2$-based S-S (Z-scheme), S-M, S-C, multicomponent, phase and facet heterojunctions.

| Photocatalyst | Reductant | Light source | Generation rate of main products ($\mu mol \cdot g_{cat}^{-1} \cdot h^{-1}$) | Quantum efficiency (%) | References |
|---|---|---|---|---|---|
| Indirect Z-scheme heterojunction | | | | | |
| $CdS/rGO/TiO_2$ | $H_2O$ vapor | 300 W Xe lamp | $CH_4$: 0.12 ($\mu mol \cdot h^{-1}$) | - | Kuai et al. (2015) |
| $CuGaS_2$-RGO-$TiO_2$ | $Na_2S$ aqueous solution | 300 W Xe lamp ($\lambda$ > 330 nm) | CO: 0.15<br>$H_2$: 28.8 ($\mu mol \cdot h^{-1}$) | - | Takayama et al. (2017) |
| Al–O Linked porous-g-$C_3N_4$/$TiO_2$-nanotube (PCN/TNT) | $Na_2SO_4$ aqueous solution | 150 W Xe lamp | $CH_3COOH$<br>HCOOH<br>$CH_3OH$ | - | Wu et al. (2019) |
| $ZnFe_2O_4$/Ag/$TiO_2$ nanorods | $H_2O$ vapor | 200 W Hg lamp | CO: 1025<br>$CH_4$: 132<br>$CH_3OH$: 30.8<br>$C_2H_6$: 19.1 ($\mu mol \cdot h^{-1}$) | - | Tahir (2020) |
| g-$C_3N_4$/Pt/3DOM-$TiO_2$@C | $H_2O$ vapor | 300 W Xe lamp ($\lambda \geq$ 420 nm) | CO: 1.47<br>$CH_4$: 6.56<br>$H_2$: 0.82 | 5.67 | Wang et al. (2020a) |
| (Au/A-$TiO_2$)@g-$C_3N_4$ | $H_2O$ vapor | 300 W Xe lamp ($\lambda \geq$ 420 nm) | $CH_4$: 37.4<br>CO: 21.7 | 1.91 | Wang et al. (2020b) |
| Direct Z-scheme heterojunction | | | | | |
| $Cu_2O/TiO_2$ | $H_2O$ vapor | 1 kW high-pressure Hg (Xe) arc lamp ($\lambda \geq$ 305 nm) | CO: 2.11 | - | Aguirre et al. (2017) |
| $ZnIn_2S_4/TiO_2$ | $H_2O$ vapor | 300 W Xe lamp | $CH_4$: 1.135 | - | Yang et al. (2017) |
| $TiO_2/CuInS_2$ | $H_2O$ vapor | 350 W Xe lamp | $CH_4$: 2.5 | - | Xu et al. (2018b) |
| $TiO_2$/CdS | $H_2O$ vapor | 300 W Xe lamp | $CH_4$: 11.9 $\mu mol \cdot h^{-1} \cdot m^{-2}$ | - | Low et al. (2019) |
| $Zn_3In_2S_6/TiO_2$ | $H_2O$ vapor | 300 W Xe lamp | $CH_4$: 6.19<br>CO: 23.35 | - | She et al. (2018) |
| Nb-$TiO_2$/g-$C_3N_4$ | $H_2O$ vapor | Two 30 W white bulbs | $CH_4$: 562<br>CO: 420<br>HCOOH: 698 | - | Thi Thanh Truc et al. (2019) |
| Copper (II)-porphyrin zirconium metal-organic framework (PCN-224(Cu))/$TiO_2$ | $Na_2SO_4$ aqueous solution | 300 W Xe lamp | CO: 37.21 | - | Wang L. et al. (2019) |
| $WO_3$-$TiO_2$/$Cu_2ZnSnS_4$ | $H_2O$ vapor | 400 W Xe lamp ($\lambda$ > 420 nm) | $CH_4$: 1.69<br>CO: 15.37 | 0.52 | Raza et al. (2020) |
| Au-$TiO_2$ | $H_2O$ vapor | AM1.5 G simulated sunlight | $CH_4$: 302 | - | Zeng et al. (2020) |
| | | 50 W white cold LED light ($\lambda$ > 400 nm) | HCHO: 420<br>CO: 323 | - | |
| Single metal | | | | | |
| 3DOM Au/$TiO_2$ | $H_2O$ vapor | 300 W Xe lamp | $CH_4$: 2.89 | - | Jiao et al. (2015) |
| $Pt^{2+}$-$Pt^0/TiO_2$ | $H_2O$ vapor | 300 W Xe lamp | $H_2$: 394.7<br>$CH_4$: 37.78<br>CO: 8.03 | 0.36 | Xiong et al. (2015) |
| Ag/$TiO_2$ | $H_2O$ vapor | 300 W Xe lamp | $CH_4$: 1.40 | 0.16 (400 nm); 0.013 (520 nm) | Yu et al. (2016) |
| Ag/$TiO_2$ nanorod arrays | $H_2O$ vapor | 300 W Xe lamp ($\lambda$ > 420 nm) | $CH_4$: 1.13<br>CO: 12 | - | Cheng et al. (2017) |
| Pt/$TiO_2$<br>Pt/$TiO_2$-COK-12 | $H_2O$ vapor | Four 6 W lamps ($\lambda \leq$ 365 nm) | $CH_4$<br>CO | - | Tasbihi et al. (2018a) |
| Ag/$TiO_2$ nanotube arrays (TNTAs) | $H_2O$ vapor | 300 W Xe lamp | $CH_4$ | - | Low et al. (2018) |
| Pt/$TiO_2$-$Al_2O_3$ foam | $H_2O$ vapor | UV 8 W Hg lamp | $H_2$: 22.5<br>$CH_4$: 1.21<br>CO: 0.54 | - | Tasbihi et al. (2018b) |
| Au-$TiO_2$ Nanotubes (TNTs) | $H_2O$ vapor | 300 W Xe lamp | $CH_4$: 14.67% | - | Khatun et al. (2019) |
| Au/$TiO_2$ | $H_2O$ vapor | 300 W Xe lamp | $CH_4$: 70.34<br>CO: 19.75 | - | Wang R. et al. (2019) |
| Au/$TiO_2$ | $H_2O$ vapor | 300 W Xe lamp | $CH_4$: 0.2<br>CO: 1.2 | - | Wang et al. (2021) |
| Metal alloy | | | | | |
| (Au, Cu)/$TiO_2$ | $H_2O$ vapor | AM1.5 G simulated sunlight | $H_2$: 286<br>$CH_4$: 2200 ± 300 | - | Neaţu et al. (2014) |

(Continued on following page)

**TABLE 3 |** (*Continued*) Photocatalytic $CO_2$ reduction performance on typical $TiO_2$-based S-S (Z-scheme), S-M, S-C, multicomponent, phase and facet heterojunctions.

| Photocatalyst | Reductant | Light source | Generation rate of main products ($\mu mol \cdot g_{cat}^{-1} \cdot h^{-1}$) | Quantum efficiency (%) | References |
|---|---|---|---|---|---|
| $AgPd/TiO_2$ | Triethylamine (TEA) aqueous solution | 300 W Xe lamp | $H_2$: 144.5<br>$CH_4$: 79.0 | - | Tan et al. (2018) |
| $PtRu/TiO_2$ | $H_2O$ vapor | 300 W Xe lamp | $H_2$: 16.5<br>$CH_4$: 38.7<br>CO: 2.6 | 0.98 | Wei Y. et al. (2018) |
| Hierarchical urchin-like yolk@shell $TiO_{2-x}H_x$ (HUY@S-TOH)/AuPd | $H_2O$ (liquid) | 300 W Xe lamp | $CH_4$: 47.0 | - | Ziarati et al. (2020) |
| Graphene and its derivatives | | | | | |
| Graphene-$TiO_2$ | $H_2O$ vapor | 300 W Xe lamp | $CH_4$: 8<br>$C_2H_6$: 16.8 | - | Tu et al. (2013) |
| RGO/Pt-$TiO_2$ nanotubes (TNTs) | $H_2O$ vapor | 500 W tungsten-halog--en lamp | $CH_4$: 10.96 ($\mu mol \cdot m^{-2}$) | - | Sim et al. (2015) |
| $TiO_2$/Nitrogen doped rGO (NrGO) | $H_2O$ vapor | 400 W Xe lamp | CO: 50 | 0.0072 | Lin et al. (2017) |
| GO/oxygen rich $TiO_2$ ($OTiO_2$) | $H_2O$ vapor | 300 W Xe lamp | $CH_4$: 0.43 | 0.0103 | Tan et al. (2017) |
| rGO/$TiO_2$ | $H_2O$ vapor | 500 W Hg lamp | $CH_4$: 12.75<br>CO: 11.93 | - | Shehzad et al. (2018a) |
| (($Pt/TiO_2$)@rGO) | $H_2O$ vapor | 300 W Xe lamp | $H_2$: 5.6<br>$CH_4$: 41.3<br>CO: 0.4 | 1.93 | Zhao Y. et al. (2018) |
| Graphene quantum dots (GQDs)/$TiO_2$ | $H_2O$ vapor | 100 W Xe solar simulator | $CH_4$: 1.98 ($ppm \cdot cm^{-2} \cdot h^{-1}$) | - | Zubair et al. (2018) |
| rGO/$TiO_2$ | Triethanolamine (TEOA) aqueous solution | 8 W UV-A lamp | $CH_3OH$: 2330 | - | Olowoyo et al. (2019) |
| CNT | | | | | |
| MWCNT/$TiO_2$ | $H_2O$ vapor | 15 W UV lamp | $CH_4$: 11.74<br>HCOOH: 18.67<br>$C_2H_5OH$: 29.87 | - | Xia et al. (2007) |
| MWCNT/$TiO_2$ | $H_2O$ (liquid) | 15 W energy saving light bulb | $CH_4$: 0.17 | - | Gui et al. (2014) |
| Ag-MWCNT@$TiO_2$ | $H_2O$ vapor | 15 W energy saving light bulb | $CH_4$: 0.91<br>$C_2H_6$: 0.048 | - | Gui et al. (2015) |
| MWCNT/$TiO_2$ | TEOA aqueous solution | 8 W UV-A lamp | $H_2$: 2360.0<br>$CH_3OH$: 3246.1<br>HCOOH: 68.5 | - | Olowoyo et al. (2019) |
| CNT/$TiO_2$/Cu | $H_2O$ vapor | 300 W Xe lamp | $CH_4$: 1.1<br>CO: 8.1 | - | Rodríguez et al. (2020) |
| Other carbon forms | | | | | |
| Carbon@$TiO_2$ hollow spheres | $H_2O$ vapor | 300 W Xe lamp | $CH_4$: 4.2<br>$CH_3OH$: 9.1 | - | Wang et al. (2017) |
| N, S-containing carbon quantum dots (NCQDs)/$TiO_2$ | $H_2O$ vapor | 300 W Xe lamp | $CH_4$: 0.13<br>CO: 0.19 | - | Li et al. (2018) |
| Carbon nanofibers@$TiO_2$ | $H_2O$ vapor | 350 W Xe lamp | $CH_4$: 13.52 | - | Zhang J. et al. (2018) |
| MgO-Pt-$TiO_2$ | $H_2O$ vapor | 100 W Xe lamp | $H_2$: 14<br>$CH_4$: 1.2<br>CO: 1.8 | - | Xie et al. (2014) |
| Pt-rGO-$TiO_2$<br>Pd-rGO-$TiO_2$<br>Ag-rGO-$TiO_2$<br>Au-rGO-$TiO_2$ | $H_2O$ vapor | 15 W energy saving light bulb | $CH_4$: 0.28<br>$CH_4$: 0.20<br>$CH_4$: 0.17<br>$CH_4$: 0.13 | - | Tan et al. (2015) |
| Pt-$Cu_2O/TiO_2$ | $H_2O$ vapor | 300 W Xe lamp | $CH_4$: 1.42<br>CO: 0.05 | - | Xiong et al. (2017c) |
| $WSe_2$-Graphene-$TiO_2$ | $Na_2SO_3$ aqueous solution | 300 W Xe lamp | $CH_3OH$: 6.33 | - | Biswas et al. (2018) |
| Pt/MgAl layered double oxides (MgAl-LDO)/$TiO_2$ | $H_2O$ (liquid) | 300 W Xe lamp | $CH_4$: 1.42<br>CO: 2.3 | - | Chong et al. (2018) |
| $TiO_2$-Graphene few-layered $MoS_2$ | $H_2O$ vapor | 300 W Xe lamp | CO: 92.33 | - | Jung et al. (2018) |
| $Au/Al_2O_3/TiO_2$ | $H_2O$ vapor | 450 W Xe lamp | CO: 11.8 | - | Zhao H. et al. (2018) |
| $TiO_2$-$MnO_x$-Pt | $H_2O$ vapor | 350 W Xe lamp | $CH_4$: 34.67<br>$CH_3OH$: 30.33 ($\mu mol \cdot m^{-2} \cdot h^{-1}$) | - | Meng et al. (2019) |
| Ag-MgO-$TiO_2$ | $H_2O$ vapor | 300 W Xe lamp | $CH_4$: 0.86<br>$CH_3OH$: 0.06 | 0.091 | Xu et al. (2018a) |
| Au@$TiO_2$ hollow spheres (THS)@CoO | $H_2O$ vapor | 300 W Xe lamp | $CH_4$: 13.3 | - | Zhu et al. (2019) |

(Continued on following page)

**TABLE 3 |** (*Continued*) Photocatalytic $CO_2$ reduction performance on typical $TiO_2$-based S-S (Z-scheme), S-M, S-C, multicomponent, phase and facet heterojunctions.

| Photocatalyst | Reductant | Light source | Generation rate of main products ($\mu mol \cdot g_{cat}^{-1} \cdot h^{-1}$) | Quantum efficiency (%) | References |
|---|---|---|---|---|---|
| Phase heterojunction | | | | | |
| Anatase-rutile $TiO_2$ fibers | $H_2O$ vapor | Four 6 W UV lamps | CO: 10.19<br>$CH_4$: 1.34<br>$H_2$: 19.94 | 0.036 | Reñones et al. (2016) |
| Anatase-rutile $TiO_2$ nanoparticles with oxygen vacancy | $H_2O$ vapor | 300 W Xe lamp | $CH_4$: 43.2 | - | Xiong et al. (2020) |
| Disordered Anatase/ordered rutile ($A_d$/$R_o$) $TiO_2$ nanoparticles | $H_2O$ vapor | Solar simulator 1 Sun | $CH_4$: 3.98<br>CO: 3.02 | 0.273 | Hwang et al. (2019) |
| Pt-loaded anatase-rutile $TiO_2$ nanoparticles | $H_2O$ vapor | 200 W Hg–Xe light | $CH_4$<br>CO | - | Lee et al. (2016) |
| N-doped carbon coating paragenetic anatase/rutile heterojunction | TEOA and MeCN | 300 W Xe lamp | CO: 24.31 | - | Chen et al. (2020) |
| $SrCO_3$-Modified brookite/anatase $TiO_2$ heterojunction | $H_2O$ vapor | 300 W Xe lamp | $CH_4$: 19.66<br>CO: 2.64 | - | Jin et al. (2019) |
| Facet heterojunction | | | | | |
| {101}/{001} $TiO_2$ | $H_2O$ vapor | 300 W Xe lamp | $CH_4$: 1.35 | - | Yu et al. (2014) |
| Oxygen-deficient {101}/{001} $TiO_2$ | $H_2O$ vapor | 100 W Hg lamp/450 W Xe lamp | CO: ~10.91 (UV-vis)<br>CO: ~5.36 (visible) | 0.31 (UV-vis)<br>0.134 (visible) | Liu L. et al. (2016) |
| Pt-loaded {101}/{001} $TiO_2$ | 0.1 M $KHCO_3$ solution | 250 W Hg lamp | $CH_4$: 4.0 | - | Cao et al. (2016) |
| Pt-loaded {101}/{001} $TiO_2$ | $H_2O$ vapor | 300 W Xe lamp | $CH_4$: 4.6<br>$H_2$: 9.9 | - | Xiong et al. (2017a) |
| Graphene supported {101}/{001} $TiO_2$ | $H_2O$ vapor | 300 W Xe lamp | CO: 70.8<br>$CH_4$: 27.4 | CO: 0.0557 $CH_4$: 0.0864 | Xiong et al. (2016) |

in $AlCl_3$ solution followed by calcination to obtain Al-O-modified TNTs, which is then combined with porous g-$C_3N_4$ (PCN) *via* solid sublimation and transition of urea/$NaHCO_3$ hybrid to from Al-O linked PCN/TNT composites. Results show that the low charge transfer efficiency at the interface between $TiO_2$ and g-$C_3N_4$ caused by lattice mismatch of the two components can be significantly improved by introducing Al-O links to replace surface hydroxyl groups, thereby enhancing the separation efficiency of photogenerated charge carriers and benefiting for photoreduction of $CO_2$ with increased yields of acetic acid, formic acid and methanol. According to Kuai's research, rGO could also serve as electron mediator for the construction of Z-scheme heterojunction between $TiO_2$ and CdS (Kuai et al., 2015). The remarkably prolonged photoluminasence (PL) decay time of CdS/rGO/$TiO_2$ (2.4 ns) reveals the different electron migration mechanism compared to CdS/$TiO_2$ (0.38 ns), which follows the carrier transfer mode in type II heterojunction. Obviously, the presence of rGO leads to the establishment of Z-scheme system, in which photogenerated electrons in the CB of $TiO_2$ are extracted by rGO and then transferred to the VB of CdS to recombine with photogenerated holes there, resulting in the enrichment of photogenerated electrons and holes in the CB of CdS and the VB of $TiO_2$, respectively. Although the photoreduction efficiency of $CO_2$ is still low on CdS/rGO/$TiO_2$, the attempt to construct Z-scheme heterojunction with low-cost carbon material instead of noble metal as electron mediator is successful, while the high selectivity for $CH_4$ generation is also promising.

Recently, construction of direct Z-scheme system by coupling two different semiconductors with matching geometric and band structure has become research hotspot in the field of photocatalytic $CO_2$ reduction, which is more facile to synthesis and more convenient for charge transfer at the interface. In particular, semiconductors with narrow band gap are more preferred in the $TiO_2$-based direct Z-scheme heterojunction to improve the utilization of visible light. Typically, $ZnInS_2$ nanosheets were decorated onto the surface of 1D $TiO_2$ nanobelts *via* hydrothermal process (Yang et al., 2017). The authors claimed the Z-scheme electron transfer mechanism between $ZnInS_2$ and $TiO_2$ based on the experimental results of $CH_4$ generation. Since the CB potential of $TiO_2$ is lower than the redox potential of $CO_2$/$CH_4$, it is reasonable to believe that photogenerated electrons in the CB of $ZnInS_2$ are retained due to the Z-scheme electron transfer mechanism and take in charge for photocatalytic $CO_2$ reduction to produce $CH_4$. However, stronger evidence is needed to prove this conjecture. In another work, a similar 3D hierarchical nanostructure was constructed by depositing $CuInS_2$ nanoplates on $TiO_2$ nanofibers (Xu et al., 2018b). DFT calculations revealed the higher Fermi level ($E_F$) of $CuInS_2$ than that of $TiO_2$, which forces electrons transfer from $CuInS_2$ to $TiO_2$ after their contact and creates a build in internal electric filed at the

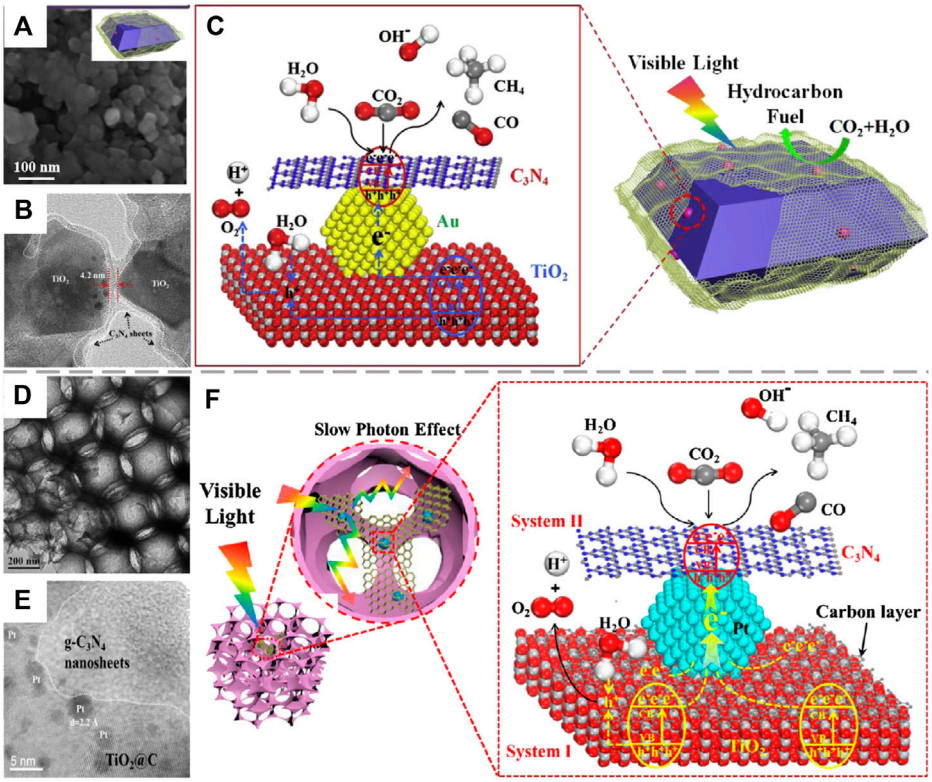


**FIGURE 5 | (A)** SEM and **(B)** HRTEM images of (Au/A-$TiO_2$)@g-$C_3N_4$ catalyst; **(C)** Schematic for photocatalytic $CO_2$ reduction with $H_2O$ to produce $CH_4$ and CO over (Au/A-$TiO_2$)@g-$C_3N_4$. Reproduced from Wang et al., 2020a with permission from Elsevier and Copyright Clearance Center. **(D)** TEM and **(E)** HRTEM images of 3DOM-CNPTC photocatalyst; **(F)** The mechanism of 3DOM-CNPTC catalyst for photocatalytic $CO_2$ reduction with $H_2O$ to $CH_4$. Reproduced from Wang et al. (2020) with permission from Elsevier and Copyright Clearance Center.

interface. The recombination of photogenerated electrons in the CB of $TiO_2$ and photogenerated holes in the VB of $CuInS_2$ under the guidance of the internal electric filed leads to the accomplishment of high efficient Z-scheme charge transfer pathway. As a result, photogenerated electrons enriched in the CB of $CuInS_2$ facilitate the photocatalytic reduction of $CO_2$ to produce $CH_4$ and $CH_3OH$ in the presence of protons provided by water oxidation. *In situ* irradiated X-ray photoelectron spectroscopy (ISI-XPS) was also applied to provide direct evidence of Z-scheme electron transfer mechanism (Low et al., 2019). The binding energy shifts of Ti 2p (by 0.3 eV) and Cd 3 days (by -0.2 eV) under light irradiation indicate the decreased electron density of $TiO_2$ as well as the increased electron density of CdS, suggesting that photogenerated electrons migrates from $TiO_2$ to CdS, which agrees well with Z-scheme mechanism. The ternary semiconductor of $Zn_3In_2S_6$ was also used by She et al. for the construction of direct Z-scheme heterojunction with $TiO_2$ (She et al., 2018). Higher CO and $CH_4$ yields were realized on $Zn_3In_2S_6/TiO_2$ in comparison with $ZnInS_2/TiO_2$ and $CuInS_2/TiO_2$, which could be attributed to the higher crystallinity of the two constituents that favored for charge separation (shown in **Figure 6**). In addition, modification on $TiO_2$ to narrow its band gap for the improved visible light adsorption is also an efficient strategy to further enhance the photocatalytic performance of the $TiO_2$-based Z-scheme heterojunction. As reported by Truc et al., $E_g$ of $TiO_2$ (3.2 eV) was reduced to 2.91 eV after Nb doping (Thi Thanh Truc et al., 2019). The as-obtained Nb-$TiO_2$ was grinded with melamine followed by calcination at 550 °C to form Nb-$TiO_2$/g-$C_3N_4$ heterojunction with a clear boundary at the interface. The well matched lattice spacing of the $TiO_2$ {101} (0.353 nm) and g-$C_3N_4$ {002} (0.320 nm) facets benefits to the electron transfer at the interface following Z-scheme mechanism, resulting in high efficiency for photocatalytic $CO_2$ reduction. The advantages of low cost, full visible light spectrum responsibility (400–700 nm) and superior generation rate of $CH_4$ (562 μmol $g_{cat}^{-1}$ $h^{-1}$), CO (420 μmol $g_{cat}^{-1}$ $h^{-1}$) and HCOOH (698 μmol $g_{cat}^{-1}$ $h^{-1}$), make Nb-$TiO_2$/g-$C_3N_4$ a promising VLD photocatalyst for practical application in the future to reduce the $CO_2$ level in the atmosphere. Moreover, the high $O_2$ yield of Nb-$TiO_2$/g-$C_3N_4$ (1702 μmol $g_{cat}^{-1}$ $h^{-1}$) indicates that the artificial Z-scheme system can mimic the nature photosynthesis by green plants well.

For a long time, stability is one of the main defects facing the photocatalysts that restricts their long-term performance. The photocatalytic activity decreased continuously in the process of illumination due to photocorrosion. Construction of Z-scheme heterojunction can also protect the narrow band gap semiconductor coupled with $TiO_2$ from photo-oxidation. As

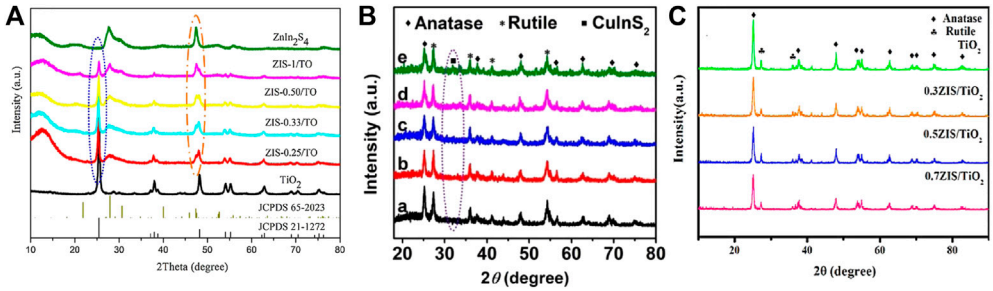


**FIGURE 6 |** XRD patterns of **(A)** $ZnInS_2/TiO_2$ series, **(B)** $CuInS_2/TiO_2$ series and **(C)** $Zn_3In_2S_6/TiO_2$ series. Reproduced from Yang et al. (2017) and Xu et al. (2018) with permission from Elsevier and Copyright Clearance Center, and She et al. (2018) with permission from Wiley-VCH, respectively.

reported by Aguirre et al., XPS spectra of $Cu_2O$ exhibited an increased Cu(II) content with the extension of illumination time, indicating that Cu(I) was partially oxidized by photogenerated holes (Aguirre et al., 2017). On the contrary, Cu(I) in the $Cu_2O/TiO_2$ heterojunction showed no obvious change in valence state, revealing the protection of $TiO_2$ toward $Cu_2O$ by injecting photogenerated electrons into the VB of $Cu_2O$ to recombine with photogenerated holes there, which also demonstrated the Z-scheme electron transfer mechanism between $TiO_2$ and $Cu_2O$. Interestingly, a stable direct Z-scheme heterojunction can also be formed between $TiO_2$ and metal organic frameworks (MOFs) as PCN-224(Cu) (Wang L. et al., 2019). It is worth nothing that the high specific surface area as well as porous structure of MOFs benefits for $CO_2$ adsorption, while the alternative ligands endow MOFs with adjustable band structure and spectra response range, thus providing a series of promising candidates for the design and construction of direct Z-scheme systems for efficient photocatalytic $CO_2$ reduction. With deepening of the research on the Z-scheme photocatalytic system and the recognition of its photocatalytic performance, more and more different types of Z-scheme photocatalysts have been developed (Raza et al., 2020; Zeng et al., 2020), accelerating the process of photocatalytic $CO_2$ reduction from basic research to practical application.

## $TiO_2$ Based S-M Heterojunction for $CO_2$ Photoreduction

As reported by previous literatures, $TiO_2$ modified by metal nanoparticles exhibits enhanced photocatalytic performance due to the promoted charge carrier separation efficiency, expanded light adsorption range as well as high selectivity toward reduction products. In general, Schottky barrier at the interface of semiconductor and metal prevents recombination of photogenerated $e^-/h^+$ pairs (Ma et al., 2014; Wang et al., 2014; Ola and Maroto-Valer, 2015; Li et al., 2019). Specifically, the higher work function of metal ($W_m$) than that of semiconductor ($W_s$) results in the higher Fermi level of semiconductor ($E_{Fs}$) than that of metal ($E_{Fm}$) (shown in **Figure 7A**). Contacting semiconductor with metal leads to charge transfer at the interface until the alignment of their Fermi levels. During the process, migration of electrons from semiconductor to metal results in band bending of the semiconductor and creates a space charge region at the interface (Schottky barrier), which could prevent backflow of photogenerated electrons to inhibit their recombination with photogenerated holes (shown in **Figure 7B**). The promoted charge separation efficiency benefits for photocatalytic $CO_2$ reduction as well as the enhanced water oxidation efficiency. In addition, metals can enrich electrons to create high electron density regions on their surfaces, which are favoring for photoreducing $CO_2$ to hydrocarbons in the presence of water due to their lower redox potential than CO. Besides, local surface plasmon resonance (LSPR) effect of certain metals can enhance visible light adsorption of the Schottky heterojunction and inject hot electrons into the CB of semiconductor, thereby facilitating the photoreduction of $CO_2$ (shown in **Figure 7C**). In this section, strategies for coupling $TiO_2$ with different metal nanoparticles as well as their different enhancement mechanisms of photocatalytic performance will be reviewed and discussed in detail. Photocatalytic $CO_2$ reduction performance of the typical $TiO_2$-based S-M heterojunctions are listed in **Table 3**.

As a classic noble metal cocatalyst, Pt has been widely used in the photocatalysis field for both water splitting and $CO_2$ reduction. In particular, $TiO_2$ loaded with Pt nanoparticles has been demonstrated to be efficient for photoreduction $CO_2$ to $CH_4$. As reported by Fresno et al., a series of $Pt/TiO_2$ photocatalysts with different Pt loading amount were fabricated by treating P25 in the Pt precursor-contained aqueous solution *via* the deposition-precipitation procedure (Tasbihi et al., 2018a). The as-obtained sample (**Figure 8A**) displays ca. 100% selectivity toward $CH_4$ generation at the optimum Pt content (>0.58 wt% of $TiO_2$), which can be ascribed to the strong chemisorption of CO on Pt nanoparticles (proved by the FTIR spectra in ATR mode (shown in **Figure 8B**) along with *in-situ* NAP-XPS analysis) and the further reduction of CO to $CH_4$ (shown in **Figure 8C**). However, the adsorption features of CO can not be observed on bare $TiO_2$, which yields CO as the main product under the same condition. The correspondingly net selectivities and quantum yield indices (QYI) are shown in **Figure 8D**. In another work, $Pt/TiO_2$ was synthesized by the hydrolysis of Titanium (IV) butoxide (TEOT) in the presence of $H_2PtCl_6{\cdot}6H_2O$, resulting in the doping of $Pt^{2+}$ into the lattice of $TiO_2$ and loading of Pt nanoparicles ($Pt^0$) on the surface of $TiO_2$ (Xiong et al., 2015). The low

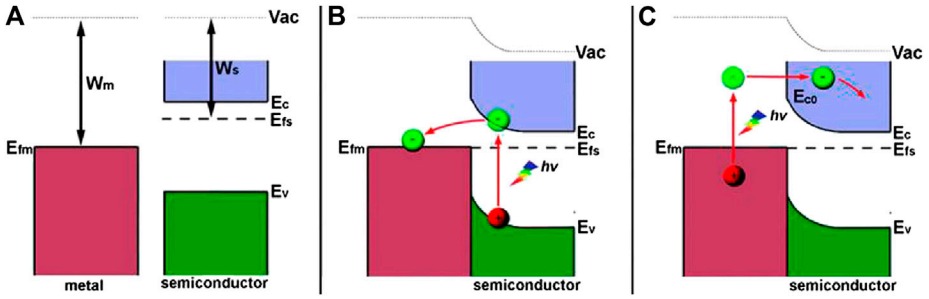


**FIGURE 7 |** Band structure of semiconductor **(A)** before contact and **(B)** after contact with metal to form the Schottky barrier; **(C)** the SPR effect induced hot electron transfer. Reproduced from Bai et al. (2015) with permission from the Royal Society of Chemistry.

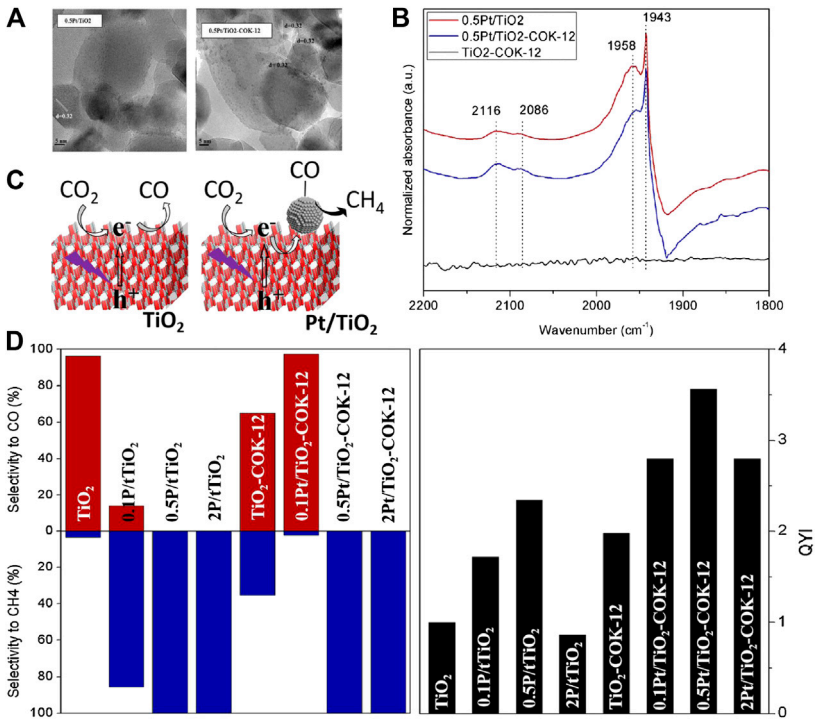


**FIGURE 8 | (A)** TEM images of 0.5 $Pt/TiO_2$ and 0.5 $Pt/TiO_2$-COK-12, **(B)** FTIR spectra of the $TiO_2$, 0.5 $Pt/TiO_2$ and 0.5 $Pt/TiO_2$-COK-12 catalysts after reaction, in the CO stretching region, **(C)** Schematic representation of the proposed reaction pathway over $TiO_2$ and $Pt/TiO_2$ catalysts, and **(D)** Net selectivities and quantum yield indices (QYI) obtained with the different catalysts. The QYI with $TiO_2$ is 1 by definition. Reproduced from Tasbihi et al. (2018a) with permission from Elsevier and Copyright Clearance Center.

recombination efficiency of photogenetated $e^-/h^+$ pairs due to the deposition of $Pt^0$ as well as strong visible light adsorption attributed to $Pt^{2+}$ doping significantly enhance photocatalytic performance of $Pt^{2+}$-$Pt^0/TiO_2$ with higher quantum yield (1.42%) for $CO_2$ conversion than that of bare $TiO_2$ (0.36%). Moreover, plenty of electrons enriched by $Pt^0$ and protons supplied by water oxidation benefit for the high selectivity toward $CH_4$ formation ($E_{red}$/SCE = −0.48 V). Compared with the formation of CO ($E_{red}$/SCE = -0.77 V), this reaction is more feasible in thermodynamics. In summary, the kinetic feasibility (strong chemisorption of CO on Pt) and thermodynamic convenience contribute to photoreduction of $CO_2$ to $CH_4$. On this basis, $Pt/TiO_2$ were deposited on porous supports with large surface area (etc. COK-12 (Tasbihi et al., 2018a) and $Al_2O_3$ foam (Tasbihi et al., 2018b)) to promote active sites exposure and achieve higher $CH_4$ yield.

Coupling $TiO_2$ with noble metals that can induce the LSPR effect has also been adapted by researchers for efficient photocatalytic $CO_2$ reduction. As reported by Wang et al., 0D/2D $Au/TiO_2$ was synthesized by *in situ* growth of Au nanoparticles on the surface of $TiO_2$ nanosheets *via* chemically reduction (Wang R. et al., 2019). The hot electrons induced by the LSPR effect of Au under visible light irradiation (550 nm) could

inject into the CB of $TiO_2$ and reduce $CO_2$ to CO. However, as the only electron source ($TiO_2$ can not be excited by visible light), the limited hot electrons cannot further reduce CO to $CH_4$. Interestingly, the Au/$TiO_2$ hybrid yielded $CH_4$ as the main product under 300 W Xe lamp irradiation that contained a certain amount of UV light. Specifically, recombination of photogenerated electrons and holes was suppressed owing to the Schottky barrier that facilitated transfer of $e^-$ from the CB of $TiO_2$ to Au. Moreover, $h^+$ remained in the VB of $TiO_2$ could oxidize water to provided plenty of protons for $CH_4$ generation. On this basis, facet engineering was introduced by Wang et al. for the rational design of interface between Au and exposed facet of $TiO_2$ to realize higher charge separation efficiency (Wang et al., 2021). Results showed that the lower height of Schottky barrier on the Au/$TiO_2${101} interface resulted in more smooth migration of photogenerated electrons from the CB of $TiO_2$ to Au compared to the Au/$TiO_2${001} interface, thereby exhibiting better performance for photocatalytic $CO_2$ reduction. Notably, the architecture of $TiO_2$ among Au/$TiO_2$ heterojunction also plays an important role for efficient photoreduction of $CO_2$ (Jiao et al., 2015; Khatun et al., 2019). Jiao et al. (Jiao et al., 2015) prepared 3D ordered macroporous (3DOM) $TiO_2$ to support Au nanopaticles, which were uniformly dispersed in the inner wall of the 3DOM structure. The multiple scattering of incident light within the 3DOM structure enhanced light utilization efficiency of the heterojunction, while the ordered macroporous also improved the mass transfer efficiency of the reactants. In addition, the SPR effect of Au induced by visible light irradiation provided extra electrons for photocatalytic $CO_2$ reduction, which was benefited for $CH_4$ generation. In another work, electrochemical anodization was used to fabricate $TiO_2$ nanotubes (TNTs) with light adsorption edge in the visible region, indicating its weak photocatalytic activity illuminated by visible light (Khatun et al., 2019). Coupling with Au by electronchemical deposition significantly improved visible light adsorption of TNTs and promoted charge separation efficiency due to the LSPR effect of Au nanoparticles. The excellent $CH_4$ yield (14.67% of $CO_2$ was converted to $CH_4$) under visible light irradiation made Au-TNTs a very promising solar-driven photocatalyst to convert $CO_2$ into hydrocarbon fuels. Similarly, plasmonic Ag were electronchemical deposited into the inner space of $TiO_2$ nanotube arrays (**Figure 9A**) to investigate the enhancement of SPR effect on photocatalytic performance, while the morphology and structure of as-obtained Ag-TNTAs-E are shown in **Figures 9B,C** (Low et al., 2018). The direct evidences of the existence of Schottky barrier between Ag and $TiO_2$ as well as migration of hot electrons induced by the SPR effect of Ag nanoparticles can be found in the synchronous-illumination X-ray photoelectron spectroscopy (SIXPS) spectra based on the shift of Ti $2p_{3/2}$ peak before and after illumination (**Figures 9D,E**). Moreover, the SPR effect of Ag nanoparticles was strengthened by the multiple scatted light in TNTAs (**Figure 9F**), while the derived near field effect accelerated charge transfer at the heterointerface to promote separation efficiency of photogenerated $e^-/h^+$ pairs, thereby endowing enhanced VLD activity of Ag-TNTAs for $CO_2$ photoreduction. Although promoting photoreduction efficiency of $CO_2$ and clarifying the involved mechanisms are the focus of current research, the improvement of photocatalyst synthesis methods also deserves attention. The silver mirror reaction was adopted by Yu et al. to deposited Ag on $TiO_2$ nanoparticles (Yu et al., 2016). $CH_3OH$ generated in $CO_2$-saturated 1 M $NaHCO_3$ solution is the main product of photocatalytic $CO_2$ reduction, which is more valuable than the primary products such as CO and $CH_4$. In another work, Ag(I) adsorbed by $TiO_2$ nanorod arrays were completely reduced by cold plasma within 30 s to form uniformly distributed Ag nanoparticles (Cheng et al., 2017). This fast and efficient strategy is very promising for the fabrication of metal nanoparticles decorated semiconductor photocatalysts on a large scale.

Bimetallic nanoalloys that combined advantages of the two metal components are efficient cocatalysts for photocatalytic $CO_2$ reduction and have been introduced in the $TiO_2$-based photocatalytic systems. As reported by Neaţu et al., Au and Cu species were deposited on $TiO_2$ nanopartcles stepwisely followed by calcining in $H_2$ atmosphere to form Au-Cu alloy (Neaţu et al., 2014). In this case, Au is served as visible light harvester due to its LSPR effect while Cu can covalently bind with CO reduced from $CO_2$ and direct the generation of $CH_4$. Therefore, high VLD photocatalytic activity with outstanding $CH_4$ selectivity (97%) was achieved. Other bimetallic nanoalloys, such as Au-Ag (Tahir et al., 2017), Au-Pd (Ziarati et al., 2020), Ag-Pd (Tan et al., 2018) and Pt-Ru (Wei Y. et al., 2018) nanoparticles are also been used to enhance photocatalytic performance of $TiO_2$ for selective reduction of $CO_2$. Among them, the combination of bimetallic nanoalloys and modified $TiO_2$ (etc. hydrogenated black $TiO_2$ ($TiO_{2-x}H_x$) (Ziarati et al., 2020) and N-doped $TiO_2$ (Tan et al., 2018)) exhibited considerably enhanced visible light utilization and charge separation efficiency, which could become the future development trend of $TiO_2$-based S-M heterojunction for solar-driven $CO_2$ photoreduction. Moreover, construction of S-M heterojunction with hierachical architecture is also in great demand (Ziarati et al., 2020).

## $TiO_2$ Based S-C Heterojunction for $CO_2$ Photoreduction

Recently, coupling $TiO_2$ with carbon-based nanomaterials including graphene and its derivatives (etc. graphene (GR) (Tu et al., 2013; Xiong et al., 2016; Biswas et al., 2018; Jung et al., 2018; Shehzad et al., 2018; Zhao et al., 2018; Zubair et al., 2018; Bie et al., 2019), graphene oxide (GO) (Chowdhury et al., 2015; Tan et al., 2017) and reduced graphene oxide (rGO) (An et al., 2014; Kuai et al., 2015; Sim et al., 2015; Tan et al., 2015; Lin et al., 2017; Olowoyo et al., 2019)), carbon nanotubes (CNTs) (Xia et al., 2007; Gui et al., 2014; Gui et al., 2015; Olowoyo et al., 2018; Rodríguez et al., 2020) and carbon quantum dots (CQDs) (Li et al., 2018; Wang K. et al., 2019) to construct $TiO_2$-carbon heterojunction for photocatalytic reduction of $CO_2$ has been widely concerned. The unique physicochemical properties of nanocarbon that responsible for the enhanced photocatalytic performance of the S-C heterojunction can be concluded as follows: 1) the large surface area and high mechanical stability of nanocarbon could provide a stable support for the uniformly distributed $TiO_2$

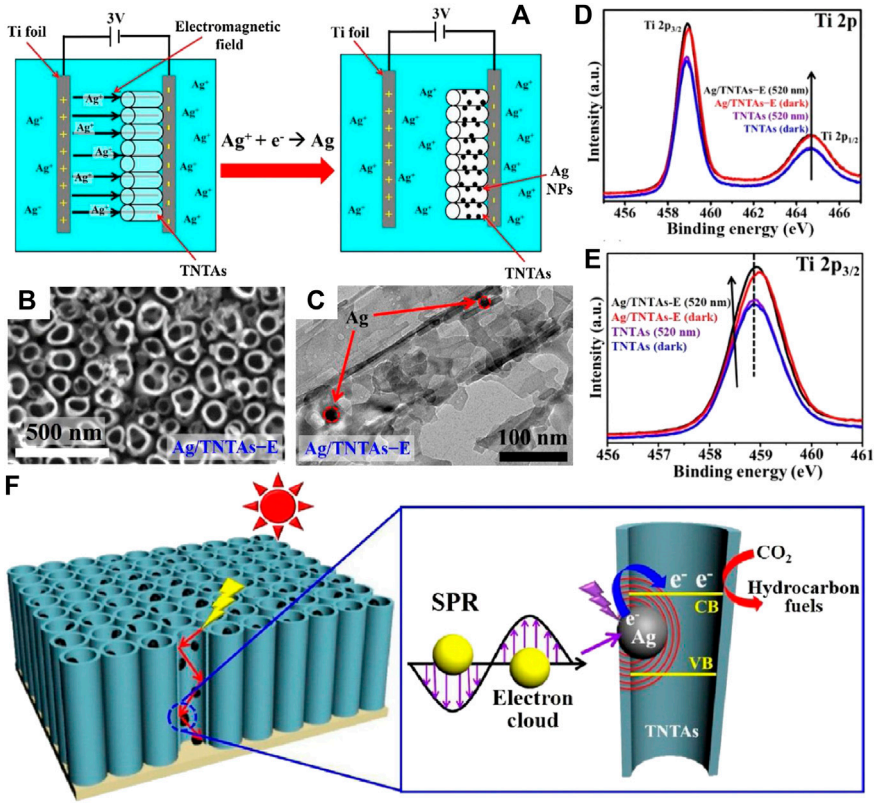


**FIGURE 9 | (A)** Schematic illustration of electrochemical deposition methods for loading Ag NPs into the TNTAs, **(B)** SEM image (top view) and **(C)** TEM image (side view) of Ag/TNTAs-E, Comparison of high-resolution SIXPS spectra of **(D)** Ti 2p and **(E)** Ti $2p_{3/2}$ for TNTAs and Ag/TNTAs-E in the dark and under 520 nm LED light irradiation, and **(F)** Schematic illustration of the enhanced SPR effect of Ag NPs in the TNTAs structure. Reproduced from Low et al. (2018) with permission from Elsevier and Copyright Clearance Center.

nanoparticles with increased exposure of active sites and enhanced $CO_2$ adsorption capacity; 2) the high charge carrier mobility, large capacitance of nanocarbon as well as the formation of Ti-O-C bond at the highly dispersed S-C interface facilitates the migration of electrons from $TiO_2$ to carbon materials, thereby enhancing the separation efficiency of photogenerated $e^-$ and $h^+$ and inhibiting their recombination; 3) the optical properties of carbon materials, such as good optical transparency and wide spectrum adsorption range (especially for CQDs, expands to near IR region), contribute to the utilization of visible light of the $TiO_2$-based S-C heterojunction and result in the improved quantum efficiency. In this section, S-C heterojunctions including $TiO_2$-GR series, $TiO_2$-CNT and $TiO_2$-CQDs are reviewed and discussed in detail, respectively. Photocatalytic $CO_2$ reduction performance of the typical $TiO_2$-based S-C heterojunctions are listed in **Table 3**.

## Coupling $TiO_2$ With Graphene and Its Derivatives

Construction of $TiO_2$-carbon heterojunction using graphene or its derivatives as the guest/host component derives improved photocatalytic performance due to its excellent electrical properties and chemical stability. It is worth nothing that the path of graphite-GO-rGO has been generally adopted by researchers to obtain graphene, whereas various of strategies have been developed for the fabrication of $TiO_2$-graphene nanocomposites. As reported by Tu et al., *in situ* simultaneous reduction-hydrolysis technique was developed for the fabrication of $TiO_2$-graphene 2D sandwich-like hybrid nanosheets (Tu et al., 2013). During the process, GO was reduced to graphene (rGO) by ethylenediamine (En) while Ti (IV) was hydrolyzed to $TiO_2$ nanoparticles and loaded on rGO through Ti-O-C bonds. The abundant surface $Ti^{3+}$ sites generated from En reduction could trap photogenerated electrons efficiently, thereby decreasing the recombination efficiency of charge carriers. Moreover, the synergism of $Ti^{3+}$ sites and garphene favors for the generation of $C_2H_6$, which is inspiring for C-C coupling during the photoreduction process of $CO_2$. In another work, the suspension of GO and $TiO_2$ in ethanol was ultrasonicated and refluxed to form Ti-O-C bonds, while GO was partially reduced to rGO during the process (Shehzad et al., 2018a). The tightly connected two phases improve charge separation at the heterointerface, while the enlarged light absorption coefficient is attributed to the reduced bandgap energy by the formation the Ti-O-C bonds. As a result, the rGO/$TiO_2$ nanocomposites exhibited greater yields of $CH_4$ (12.75 μmol $g_{cat}^{-1}$ $h^{-1}$) and CO (11.93 μmol $g_{cat}^{-1}$ $h^{-1}$) than anatase for 4 folds. Theoretical calculation was applied by Olowoyo et al. to investigate the enhanced photocatalytic performance of rGO/$TiO_2$ in reducing

$CO_2$ (Olowoyo et al., 2019). Results reveal that the high electron density of rGO has significant influence on the $TiO_2$ bands and endows visible light responsibility of the composite. Moreover, the different electron migration paths within rGO/$TiO_2$ under different light sources were observed. Compared to the electron transfer from $TiO_2$ to rGO under UVA, irradiation by visible light leads to the direct generation of electorns and holes in rGO or $TiO_2$, respectively. Both of the two pathways are efficient for photogenerated charge separation and favor for methanol production. In addition, the large adsorption capacity of $CO_2$ is another feature of $TiO_2$/graphene that contribute to photocatalytic $CO_2$ reduction (Chowdhury et al., 2015). As reported by Chowdhury et al., $TiO_2$/GO nanocomposites was obtained from the aqueous suspension of GO and $TiO_2$ under ultrasonication flowed by continuous stirring. The synergism of physisorption (intermolecular electrostatic interactions as van der Waals forces or London dispersion forces) and chemisorption (coordination of O atoms with surface Lewis acid center (Ti sites), or coordination of C atom with surface Lewis acid center (oxygen functionalities of GO or $TiO_2$)) led to the high adsorption amount of $CO_2$ (1.88 mmol $g^{-1}$), which facilitated its activation and photocatalytic reduction. Considering that photoreduction of $CO_2$ requires the participation of electrons and protons produced by photooxidation of $H_2O$, the adsorption capability of $H_2O$ molecule by photocatalyst is also critical. In view of the compete adsorption of $H_2O$ and $CO_2$ on the active sites, proper partial pressures of $CO_2$ and $H_2O$ are in great demand that determines the $CH_4$ yield on GO-doped oxygen-rich $TiO_2$ (Tan et al., 2017). Notably, the $CO_2$ adsorption capacity and charge separation efficiency can be further improved by introducing nitrogen dopants into rGO to form NrGO/$TiO_2$ system (Lin et al., 2017). On the one hand, the positive electrostatic potential regions created by nitrogen dopants on the surface of NrGO benefit for $CO_2$ adsorption and activation. On the other hand, the injection of electrons from quaternary-N species existed in NrGO matrix to the delocalized π-system facilitates the transfer of electrons and inhibits the recombination of photogenerated $e^-$/$h^+$ pairs. These findings are very helpful for the design of photocatalytic system based on heteroatom-doped graphene for $CO_2$ conversion with high efficiency. Furthermore, construction of well-defined nanostructure offers another thought to improve photocatalytic performance of $TiO_2$/graphene heterojunction (Zubair et al., 2018). Typically, $TiO_2$ nanotube arrays (TNT) with attractive 1D vectorial charge transfer can suppress recombination of photogenerated charge carriers efficiently. Graphene quantum dots (GQDs) decorated on $TiO_2$ nanotube (G-TNT) promotes charge transfer at the heterointerface, which could also enhance the light utilization of the heterojunction due to its superior visible light responsibility. Besides, the high surface area of the heterojunction contributes to the exposure of active sites that favor for $CO_2$ adsorption and activation. Consequently, a 5.6 fold $CH_4$ yield was obtained on G-TNT in comparison with pure TNT. On this basis, Pt nanoparticles were employed for the construction of rGO/Pt-TNT ternary composite with promoted visible light responsibility and photoreduction selectivity of $CO_2$ to produce $CH_4$ (Sim et al., 2015). In particular, the LSPR effect of Pt expands light adsorption range of the heterojunction to 450 nm that can be activated by visible light. Similarly, the high selectivity for $CH_4$ generation (99.1%, compared to CO yield) was also proved by Zhao et al. on (Pt/$TiO_2$)@rGO system (Zhao H. et al., 2018), in which vectorial electron transfer from $TiO_2$ to rGO through Pt was also demonstrated.

## Coupling $TiO_2$ With CNT

Generally, charge transfer along the 1D CNT leads to high separation efficiency of photogenerated $e^-$/$h^+$ pairs and endows superior photocatalytic performance of $TiO_2$/CNT heterojunction. Moreover, CNT can also serve as support to reduce the aggregation of $TiO_2$ nanoparticles, thus resulting in the formation of highly dispersed heterointerface and large exposure of active sites. As reported by Xia et al., the multi-walled CNT (MWCNT)/$TiO_2$ hybrid fabricated *via* sol-gel method yielded $C_2H_5OH$ as the main photoreduction product of $CO_2$ under UV light irradiation (Xia et al., 2007). In a further study, MWCNT/$TiO_2$ with core-shell nanostructure was demonstrated to be visible light active (due to the excellent visible light adsorption ability of CNT) that can convert $CO_2$ to $CH_4$ (Gui et al., 2014). A following work carried out by this group introduced Ag nanoparticles to MWCNT/$TiO_2$ system (Ag-MWCNT@$TiO_2$) for the further enhanced photocatalytic performance (Gui et al., 2015). In particular, the Schottky barrier between Ag and $TiO_2$ prevents backflow of photogenerated electrons that transferred from $TiO_2$ to Ag. The synergism of MWCNT and Ag nanoparticles greatly enhances separation efficiency of photogenerated charge carriers and restricts their recombination, thereby resulting in higher $CH_4$ formation rate (0.91 μmol $g_{cat}^{-1}$ $h^{-1}$) in comparison with the binary system (MWCNT@$TiO_2$, 0.17 μmol $g_{cat}^{-1}$ $h^{-1}$). Further studies revealed the mechanism of electron transfer between $TiO_2$ and CNT (Olowoyo et al., 2019). Specifically, strong attachment between MWCNT and the {101} facet of anatase $TiO_2$ introduces common orbitals within the band gap of $TiO_2$, which is the fundamental of charge transfer between the two phases and enables visible light responsibility of the composites. Electron transfer from $TiO_2$ with higher density of initial states to MWCNT under irradiation of both UVA and visible light is more probable basing on the computation results. In addition, the tight contact between MWCNT and $TiO_2$ due to the combination of sonothermal and hydrothermal methods results in extremely high photocatalytic activity with $CH_3OH$ generation rate of 2360 μmol $g_{cat}^{-1}$ $h^{-1}$, much higher than that of the similar photocatalytic systems. A recent study reported the fabrication of $TiO_2$/CNT composite in the medium of supercritical $CO_2$ (Rodríguez et al., 2020). Although photocatalytic activity of the product is relatively weak (CO, 8.1 μmol $g_{cat}^{-1}$ $h^{-1}$; $CH_4$, 1.1 μmol $g_{cat}^{-1}$ $h^{-1}$), it can also provide a novel strategy for the synthesis of $TiO_2$-based photocatalyst and leave a large space for performance improvement.

## Coupling $TiO_2$ With CQDs

As a new class of 0D carbon-based nanomaterial, the excellent photoelectric properties of CQDs, such as wide spectral response range, photo-induced charge transfer ability, up-conversion

function and anti-photocorrosion property, make it a promising cocatalyst to enhance photocatalytic performance of traditional semiconductor photocatalyst as $TiO_2$ (Li et al., 2018; Wang K. et al., 2019). As reported by Li et al., N, S-containing CQDs (NCQDs) was synthesized *via* a microwave-assisted method using thiourea and citric acid as precursors, which then assembled with P25 under continuous stirring at 80°C to form NCQDs-$TiO_2$ nanocomposites. Particularly, $TiO_2$ sensitized by NCQDs can be activated by visible light, while electrons transferred from rutile $TiO_2$ in P25 to NCQDs prevented recombination of photogenerated $e^-/h^+$ pairs, thus enhancing photoreduction efficiency of $CO_2$. Although the photoelectric properties of CQDs are attractive, relative research about coupling CQDs with $TiO_2$ or other semiconductors to construct heterostructured photocatalyst for photocatalytic $CO_2$ reduction is still few. In our opinion, as an important characteristic distinguished from other carbon-based materials, up-conversion function of CQDs is worth developing to improve the light energy utilization of heterostructured photocatalysts, especially for the wide band gap semiconductor-contained systems.

In addition to carbon-based nanomaterials analyzed above, other carbon forms can also combine with $TiO_2$ to obtain heterojunction for photocatalytic $CO_2$ reduction with high efficiency. For instance, Zhang et al. coated $TiO_2$ on electrospun carbon nanofibers to promote active sites exposure as well as charge separation and transfer of the nanocomposites (Zhang J. et al., 2018). Besides, the heat produced by carbon nanofibers due to its photothermal conversion function accelerates the diffusion kinetics of reactants and products during photocatalytic process, thus further enhancing the photoreduction efficiency of $CO_2$. The local photothermal effect induced by carbon species is also highlighted by Wang et al. among the hybrid carbon@$TiO_2$ hollow spheres (Wang et al., 2017). Moreover, the multiple scattering of incident light within the hollow structure improves light utilization of the hybrid (shown in **Figure 10**) and contributes to improve the quantum efficiency of photocatalytic $CO_2$ reduction. This result indicates that not only component, but also architecture of the heterojunction photocatalysts plays important role in improving photocatalytic performance.

## $TiO_2$ Based Multicomponent Heterojunction for $CO_2$ Photoreductions

Construction of $TiO_2$-based multicomponent heterojunction to introduce two different functional co-catalysts for efficient VLD photocatalytic $CO_2$ reduction has been widely adopted, in which $TiO_2$ combined with any two of another semiconductor (AS), metal nanoparticles (MNPs) and nanocarbon (C) to form ternary composites is currently the most studied system. Previous research revealed the highest selectivity of Pt for $CH_4$ generation compared to other noble metal cocatalysts (Pt > Pd > Au > Rh > Ag) due to its excellent electron extraction ability that derives high electron density around it and facilitates $CO_2$ photoreduction (Xie et al., 2014). However, the consequent increase in $H_2$ production is unfavorable and should be suppressed to realize further enhanced photoreduction efficiency of $CO_2$. Xie et al. coated MgO amorphous layers on Pt/$TiO_2$ hybrid to improve chemisorption of $CO_2$, which was then reduced to $CH_4$ directly by photogenerated electrons enriched on adjacent Pt nanoparticles with high efficiency, thus benefiting for the selective formation of $CH_4$. The similar function of $Cu_2O$ was demonstrated by Xiong et al. from the Pt-$Cu_2O$/$TiO_2$ nanocomposite (Xiong et al., 2017c). Notably, the charge separation efficiency of the ternary system decreased with the increasing amount of MgO, indicating that excess MgO may restrict electrons transfer from $TiO_2$ to Pt. Therefore, $TiO_2$/MNPs/AS ternary heterojunctions with rational designed architecture and efficient carrier migration path are necessary. According to Meng's research, $MnO_x$ and Pt were selectively deposited on the {001} and {101} facet of $TiO_2$ (**Figure 11A,B,C**), respectively (Meng et al., 2019). The series connection of S-M (Pt and $TiO_2${101}), facet ($TiO_2${101} and {001}) and p-n ($TiO_2${101} and $MnO_x$) heterojunction accelerated migration of photogenerated electrons along the path of MnOx→$TiO_2$ {001}→$TiO_2${101}→Pt while photogenerated holes in the opposite direction (shown in **Figure 11D,F**). As a result, the separation efficiency of photogenerated charge carriers is greatly improved, so as to the enhanced photocatalytic performance with $CH_4$ and $CH_3OH$ as the main products. In another work, Z-scheme heterojunction that is favoring for the recombination of inefficient charge carriers was constructed by coupling $TiO_2$ and $ZnFe_2O_4$ using Ag as electron mediator (Tahir, 2020). Superior CO yield (1025 $\mu mol\ g_{cat}^{-1}\ h^{-1}$) accompanied with the generation of $CH_4$ (132 $\mu mol\ g_{cat}^{-1}\ h^{-1}$) and $CH_3OH$ (31 $\mu mol\ g_{cat}^{-1}\ h^{-1}$) should be attributed to the enhanced charge separation efficiency under UV light irradiation. It is worth nothing that the magnetic properties of $ZnFe_2O_4$ should not be ignored which facilitate the recovery of photocatalyst from solid-liquid suspension, although the solid-gas mode is undertaken in this study. Moreover, Ag could also promote visible light adsorption of the ternary system due to its strong LSPR effect, which had been demonstrated by Xu et al. using MgO-Ag-$TiO_2$ as photocatalyst (Xu and Carter, 2019). In order to further investigate the synergism of the LSPR effect and chemisorption of $CO_2$ on the improvement of photoreduction efficiency of $CO_2$, $TiO_2$/MNPs/AS heterojunctions as Au/$Al_2O_3$/$TiO_2$ (Zhao Y. et al., 2018) and Au@$TiO_2$ hollow spheres (THS)@CoO (Zhu et al., 2019) were synthesized. On this basis, MgAl layered double oxides (MgAl-LDO) were developed to provide both Lewis basic sites (MgO) and Lewis acid sites ($Al_2O_3$) for $CO_2$ chemisorption and $H_2O$ dissociation among the Pt/MgAl-LDO/$TiO_2$ nanocomposite, respectively (Chong et al., 2018). Benefiting from the generation of monodentate carbonate (m-$CO_3^{2-}$) on the surface of MgO accompanied with the supply of $H^+$ from $H_2O$ dissociation by $Al_2O_3$, the activation of $CO_2$ became easier and led to the increased $CH_4$ yield by 11 folds compared to Pt/$TiO_2$.

In a typical $TiO_2$/C/AS system, nanocarbon is served as electron channel to guide photogenerated electrons flow from $TiO_2$ to the AS while photogenerated holes left in the VB of $TiO_2$, thereby resulting in the spatial separation of photoinduced redox reactions with enhanced $CO_2$ photoreduction efficiency. As reported by Jung et al., mesoporous $TiO_2$ and a few layers of

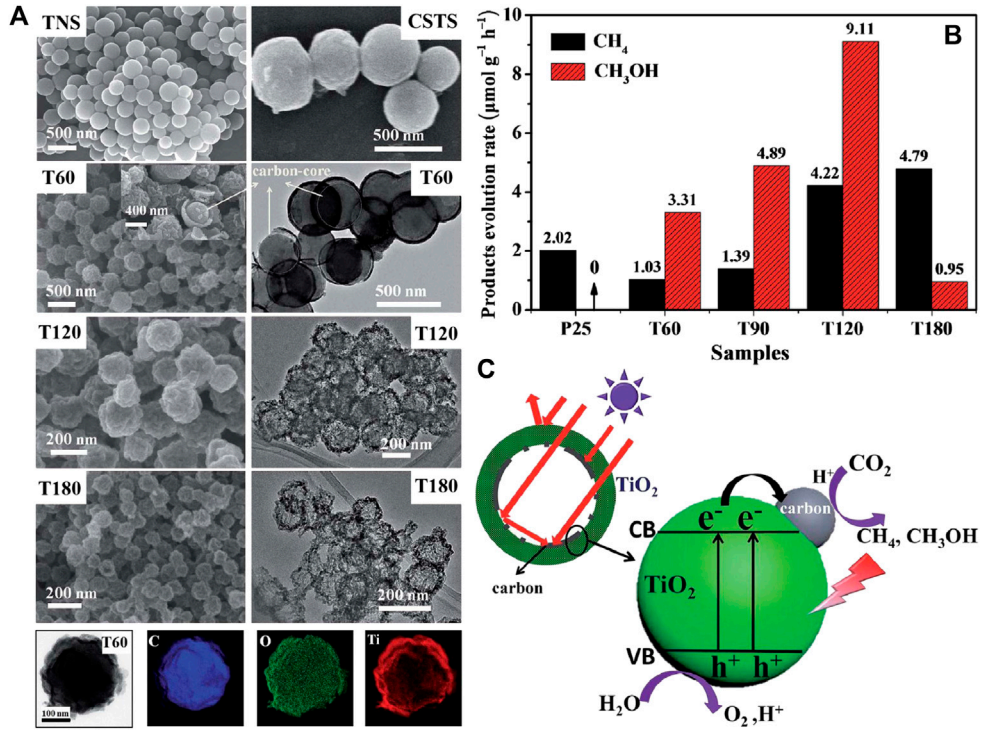


**FIGURE 10 | (A)** FESEM images of TNS, CSTS, T60, T120 and T180, and TEM images of T60, T120 and T180, and STEM image of T60 and the corresponding elemental mapping images of C, O and Ti; **(B)** Comparison of the photocatalytic $CH_4$ or $CH_3OH$ evolution rate of carbon@$TiO_2$ composite samples and P25 (under simulated solar light); and **(C)** Photoexcitation process of the carbon@$TiO_2$ composite photocatalyst with hollow structure. Reproduced from Wang et al. (2017) with permission from the Royal Society of Chemistry.

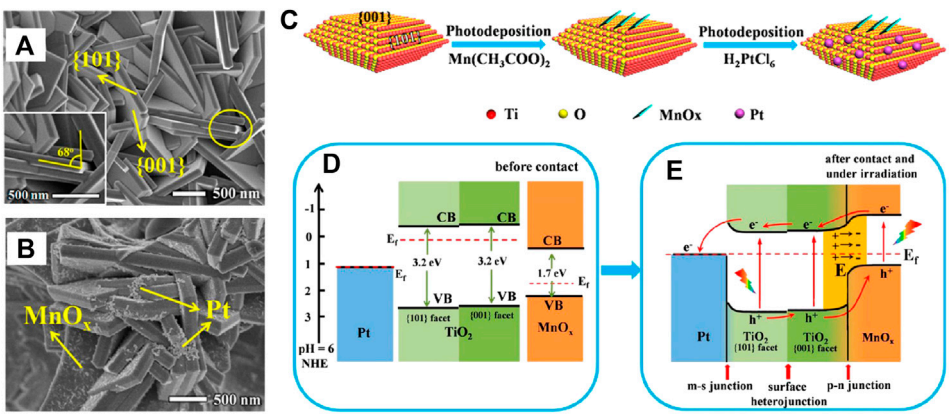


**FIGURE 11 |** SEM images of as-prepared **(A)** $TiO_2$ and **(B)** $TiO_2$-$MnO_x$-Pt (TMP); **(C)** Schematic diagram of selective photodeposition process of $MnO_x$ nanoflakes and Pt nanoparticles on anatase $TiO_2$ {001} and {101} facets; Schematic diagram of proposed photocatalytic $CO_2$ reduction mechanism of sample TMP. The relative band energy positions of $TiO_2$, Pt, and $MnO_x$ **(A)** before contact and **(B)** after contact and under irradiation. Reproduced from Meng et al. (2019) with permission from the American Chemical Society.

$MoS_2$ were assembled with graphene aerogel *via* one-pot hydrothermal method to construct a 3D hierarchical structure (Jung et al., 2018). In addition to high separation efficiency of photogenerated $e^-/h^+$ pairs, the improvement of light utilization and mass transfer efficiency based on the 3D structure of graphene with efficient visible light adsorption (Biswas et al., 2018) is also important factor that contribute to photocatalytic $CO_2$ reduction. Compared to semiconductors as $MoS_2$ (Jung et al., 2018), $CuGaS_2$ (Takayama et al., 2017) or $WSe_2$ (Biswas et al., 2018), noble metal nanoparticles are more efficient for the accumulation of photogenerated electrons transferred through electron channel (graphene) and favoring for the generation of

more valuable products as $CH_4$ and $CH_3OH$ (Tan et al., 2015; Meng et al., 2019; Tahir, 2020). However, the high cost as well as relative low resistance toward photocorrosion restricts their application on a large scale. Photocatalytic $CO_2$ reduction performance of the typical $TiO_2$-based multicomponent heterojunctions above are listed in **Table 3**. In the future, the development of noble metal-free multicomponent heterojunction based on $TiO_2$ for efficient solar-driven photocatalytic $CO_2$ reduction will become one of the main directions in this field.

## $TiO_2$ Based Phase and Facet Heterojunctions for $CO_2$ Photoreduction

### $TiO_2$ Based Phase Heterojunction

Phase heterojunction composed of different crystal phases of the same semiconductor exhibits greater photocatalytic activity than the single-phased photocatalyst (Ma et al., 2014; Wei L. et al., 2018; Nguyen et al., 2020). This is because the contact of crystal phases with different energy band structure leads to an increase in carrier separation efficiency at the interface. Moreover, the unique interfacial trapping sites may become new photocatalytic active sites. As is known, there are four main crystal phases of $TiO_2$ (including anatase, rutile, brookite, and $TiO_2$ (B)) existed in nature, in which rutile is the most thermodynamically stable phase and can be obtained by calcining the other three polymorphs (Ma et al., 2014). Among them, as the two most widely studied $TiO_2$ crystal phases with photocatalytic activity, the difference in the lattice structure of anatase and rutile leads to different electronic band structures, and ultimately results in a difference in band gap width. Compared to rutile ($E_g$ = 3.02 eV for bulk material), anatase tends to show higher photocatalytic activity due to its wider band gap ($E_g$ = 3.20 eV for bulk material) that gives stronger redox ability to the photogenerated carriers. In addition, the higher concentration of oxygen vacancies in anatase leads to more efficient charge separation, whereas the larger specific surface area leads to more active sites exposure, which are also important factors for its better photocatalytic performance than rutile. However, the narrower band gap enables rutile to respond to photons close to the visible region. Besides, the higher crystallinity results in the better charge carrier mobility within rutile. At present, the integration of the advantages of anatase and rutile to construct a phase heterojunction for photocatalytic $CO_2$ reduction has attracted increasing attention of researchers. As a classic anatase-rutile phase heterojunction, the commercial Degussa P25 has been regarded as a benchmark for both photocatalytic oxidation and reduction reactions. As reported by Reñones et al., hierarchical $TiO_2$ nanofibres composed of anatase and rutile nanoparticles were synthesized by the calcination of electrospun $TiO_2$ fibers under Ar atmosphere (Reñones et al., 2016). The phase composition of the fibers depend on the calcination conditions, in which higher rutile amount (81:19) was obtained under static Ar atmosphere (Fibers B) than the dynamic sample (Fibers A, 93:7). Notably, the faster charge transport along the grain boundaries in fibers is attributed to the improved nanocrystals connection, whereas the fibers with higher anatase content exhibits lower recombination efficiency of $e^-/h^+$ pairs, thus endowing greater photocatalytic efficiency for reducing $CO_2$ to CO (10.19 μmol $g_{cat}^{-1}$ $h^{-1}$). In addtion, the overall apparent quantum yields (AQY) of Fibers B (0.036%) is also higher than P25 (0.030%), indicating the enhanced utilization of incident light. However, the large amount of hydrogen evolution (19.94 μmol $g_{cat}^{-1}$ $h^{-1}$) during the photocatalytic process needs to be suppressed to further improve the photoreduction efficiency of $CO_2$. A hydrothermal method was developed by Xiong et al. for the fabrication of anatase-rutile heterophase $TiO_2$ nanoparticles using $K_2TiO(C_2O_4)_2{\cdot}2H_2O$ as Ti source, which simplifies the synthesis process and makes the reaction conditions more mild (Xiong et al., 2020). Ethylene glycol (EG) was added to the hydrothermal system in order to introduce oxygen vacancy into $TiO_2$ ($TiO_{2-x}$), which could trap photogenerated $e^-$ to restrain the recombination of $e^-/h^+$ pairs, thereby enhancing the photocatalytic performance of the catalysts. Electron paramagnetic resonance (EPR) spectra revealed that the concentration of oxygen vacancy increased with the increasing amount of EG during the formation process of $TiO_{2-x}$. However, the excess oxygen vacancies, especially the bulk oxygen vacancies, will act as the recombination center of carriers, resulting in the lower photocatalytic efficiency of as-obtained anatase-rutile heterojunction. Thus, the concentration and distribution of oxygen vacancies should be reasonably designed and constructed to promote the performance of the semiconductor photocatalysts. As reported by Xiong et al. (Xiong et al., 2020), the $TiO_2$-EG10 sample synthesized using 30 ml $H_2O$ and 10 ml EG as solvent exhibits the optimized photocatalytic activity in reducing $CO_2$ to $CH_4$ (43.2 μmol $g_{cat}^{-1}$ $h^{-1}$), which is 54 times higher than that of P25 (0.8 μmol $g_{cat}^{-1}$ $h^{-1}$). Usually, the optimization of oxygen vacancy concentration in photocatalyst is based on the feedback of experimental results rather than theoretical design. Therefore, the critical oxygen vacancy concentration in different photocatalytic systems is various, which is difficult to give a definite value. Considering the poor visible light responsibility of anatase/rutile phase heterojunction, it is necessary to reduce its band gap width to improve the utilization of incoming solar spectrum. In addition, the combination of disordered anatase ($A_d$) with more active sites and ordered rutile ($R_o$) for fast transport of $e^-$ and $h^+$ to suppress charge recombination can further enhance the photoreduction efficiency of $CO_2$ by $TiO_2$. On this basis, a phase-selective $A_d/R_o$ $TiO_2$ was prepared by treating P25 in the sodium alkyl amine solutions at room temperature and ambient atmosphere, in which anatase among P25 was selective reduced to produce more $Ti^{3+}$ defects (Hwang et al., 2019). The existence of multi-internal energy bands of $Ti^{3+}$ defect sites in $A_d$ reduces the band gap of $A_d/R_o$ $TiO_2$ to 2.62 eV, while the newly conduction band (-0.27 eV) is well match the redox potential of $CO_2/CH_4$ (-0.24 V vs. NHE). As a result, the VLD $A_d/R_o$ $TiO_2$ exhibits enhanced reactivity to convert $CO_2$ into $CH_4$ (3.98 μmol $g_{cat}^{-1}$ $h^{-1}$), which is higher than metal (W, Ru, Ag, and Pt)-doped P25. To further improve the $CH_4$ generation selectivity, 0.1% mass Pt was loaded on the $H_2O_2$ modified $TiO_2$ (M-$TiO_2$, containing two phases of anatase and rutile) through photoelectrodeposition (Pt/M-$TiO_2$) (Lee J. S. et al., 2016). As electron sinks, photogenerated electrons

are enriched by Pt nanoparticles and form high charge density areas near their surface, which is favoring for the photoreduction of $CO_2$ to $CH_4$ in cooperation with sufficient protons generated by water oxidation. Notably, the yield of $CH_4$ on Pt/M-$TiO_2$ is about 60 times that of bare M-$TiO_2$, whereas no CO formation can be observed, indicating its high selectivity toward photoreduction products of $CO_2$. Compared with the common method that fabricates phase heterojunction by calcining $TiO_2$ gel, the MOFs ($NH_2$-MIL-125) derived method was adopted by Chen et al. (Chen et al., 2020) to fabricate anatase-rutile junction with large surface area and porous structure that favored for $CO_2$ adsorption. Besides, the *in situ* phase transformation from anatase (211) plane to rutile (211) plane results in the highly dispersed anatase/rutile interface for efficient interfacial charge separation, inhibiting the recombination of photogenerated $e^-/h^+$ pairs significantly. Moreover, the N-doped carbon layer (generated by the pyrolysis of organic ligands) coating on the anatase/rutile heterostructure promotes the electric conductivity of the photocatalytic system, and expandes its light absorption range to 700 nm. The synergism of N-doped carbon and paragenetic anatase/rutile heterostructure derives the enhanced photoreduction efficiency of $CO_2$ to CO, which is 7.6 folds compared with P25. Although the added value of the product (CO) is limited, this method has guiding significance for the design and synthesis of other MOFs derived heterostructured photocatalytic systems. In addition to rutile, anatase can also form a phase heterojunction with brookite for photocatalytic $CO_2$ reduction (Jin et al., 2019). Generally, $Sr^{2+}$ ions were introduced to the $TiCl_4$-involed hydrothermal system for the fabrication of $SrCO_3$-modified brookite/anatase $TiO_2$ heterophase junctions (HPJs). Similar to the anatase-rutile system, the interfacial electron transfer from brookite to anatase promotes the photogenerated charge separation. Moreover, the surface modification of HPJs by $SrCO_3$ can improve the adsorption of $CO_2/H_2O$, which can also serve as an efficient cocatalyst for the selective reduction of $CO_2$ to $CH_4$. Especially, 1.0 w/w% $SrCO_3$/HPJs composite shows the selectivity of ca. 7.45 for $CH_4$/CO (19.66/2.64 μmol $g_{cat}^{-1}$ $h^{-1}$), which is ca. 32.4 folds compared with pristine brookite $TiO_2$ (0.79/3.46 μmol $g_{cat}^{-1}$ $h^{-1}$). This work can also provide guidance for the development of heterojunctions composed of $TiO_2$ HPJs and alkaline earth metal carbonates *via* a facile one pot hydrothermal route.

## $TiO_2$ Based Facet Heterojunction

The difference of geometrical and electronic structures between different crystal facets of the same semiconductor results in the distinctness of their photocatalytic activity. Facet engineering has been applied to control the exposed crystal facet of semiconductors, in order to increase the exposure of active sites and promote the adsorption and activation of substrates, so as to achieve enhanced photocatalytic performance. In terms of anatase $TiO_2$, the {101} has the lowest surface energy (0.44 J $m^{-2}$) among the low-index facets (including {001}, {010} and {101}) and dominant for $CO_2$ adsorption basing on first-principles calculations (Yu et al., 2014). The photogenerated electrons transferred from the {101} of $TiO_2$ to $CO_2$ facilitates its activation and reduction. Moreover, the enriched photogenerated holes on the {001} of $TiO_2$ can accelerate the oxidation reactions. Photocatalytic $CO_2$ reduction over anatase $TiO_2$ with coexposed {001} and {101} facets was reported by Yu et al. for the first time with the propose of "facet heterojunction" concept (Yu et al., 2014). The facet ratio of {001} and {101} can be tuned by adjusting the amount of HF during the fabrication process, as see in **Figures 12A,B**, while the correspondingly schematic illustration is displayed in **Figure 12C**. In particular, the formation of facet heterojunction between {001} and {101} contributes to the transfer and separation of photogenerated carriers, which is beneficial to the enrichment of $e^-$ and $h^+$ on {101} and {001}, respectively (shown in **Figure 12D**). As a result, photocatalytic $CO_2$ reduction occurs selectively on the {101} facet, while the optimized photocatalytic performance is realized when the facet ratio of {101} to {001} is 45–55, in which $CO_2$ is reduced to $CH_4$ with a generation rate of 1.35 μmol $g_{cat}^{-1}$ $h^{-1}$ (**Figure 12E**). On this basis, oxygen vacancies were introduced to the {101} and {001} facets coexposed anatase $TiO_2$ for the further enhancement of photocatalytic performance, where $TiO_2$ fabricated *via* hydrothermal route in the presence of HF was reduced by $NaBH_4$ to generate surface oxygen defects (Liu L. et al., 2016). In addition to the high charge separation efficiency at the interface of {001} and {101} facets, the visible light responsibility attributed to the newly generated $Ti^{3+}$ energy state as well as the improved $CO_2$ adsorption and activation derived from the synergism of $Ti^{3+}$ and oxygen vacancies resulted in the enhanced photoreduction efficiency of $CO_2$. An explicit atomistic model of the interface was applied for further investigation of charge transfer between coexposed {101} and {001} facets of anatase $TiO_2$ (Di Liberto et al., 2019). The first principles calculations revealed that the localization of $h^+$ on oxygen ion of the {001} side and the migration of $e^-$ to Ti ion of the {101} side promoted the charge separation and suppressed their recombination, hence responsible for the enhanced photocatalytic activity of the facet junction. In another work, HF was also used by Cao et al. (Cao et al., 2016) for tuning the ratio of coexposed {101} and {001} facets of anatase $TiO_2$ in a hydrothermal system where nanotube titanic acid (NTA) was used as precursor to facilitate the mass transfer of HF, thereby simplifying the generation of {001} facet. Notably, the anatase $TiO_2$ nanocrystals with coexposed 51% {001} and 49% {101} facets exhibit the highest photocatalytic activity for reducing $CO_2$ to $CH_4$ (1.58 μmol $g_{cat}^{-1}$ $h^{-1}$) among pure $TiO_2$ series, which can be further improved to 4.0 μmol $g_{cat}^{-1}$ $h^{-1}$ by decorating 1wt% $Pt^0$ nanoparticles on their surfaces. The effect of Pt loading for the enhanced photocatalytic performance of anatase $TiO_2$ facet heterojunction ({101}/{001}) was further investigated by Xiong et al. (Xiong et al., 2017a). Pt precursors ($H_2PtCl_6$ or Pt $(NH_3)_4Cl_2$) and deposition methods (photodeposition or chemical reduction) had significant influence on size, distribution, and valence states of Pt nanoparticles, hence led to the difference of photocatatic performance. In particular, the well dispersed Pt nanoparticles fabricated by chemical reducing $H_2PtCl_6$ (HC) possessed suitable particle size and high $Pt^0/Pt^{II}$ ratio (1.15), which led to efficient separation of photogenerated carriers and high efficiency for photoreduction $CO_2$. Coupling

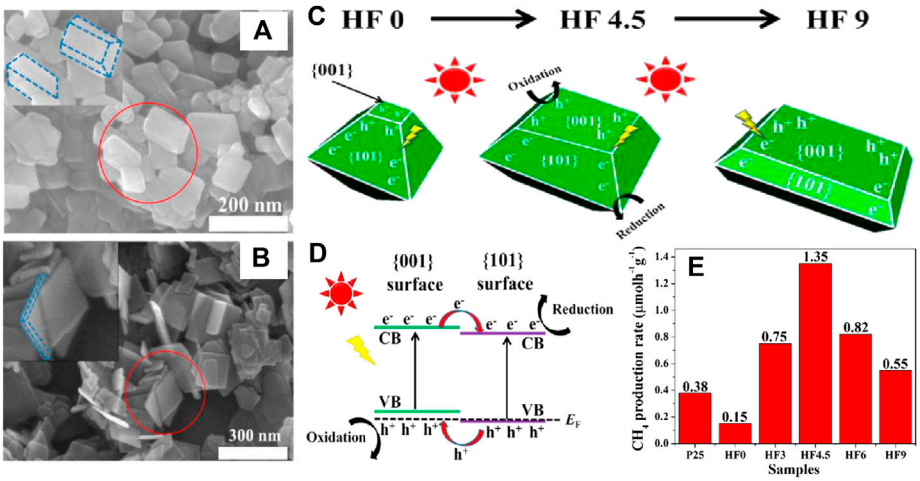


**FIGURE 12 |** FESEM images of **(A)** HF4.5 and **(B)** HF9; Schematic illustration of **(C)** tuning the ratio of {101} to {001} facets of anatase $TiO_2$ by adjusting the amount of HF, and **(D)** charge transfer at the interface of {101}-{001} facet heterojunction of anatase $TiO_2$; **(E)** Comparison of the photocatalytic $CH_4$-production activity of P25 and the $TiO_2$ samples prepared by varying HF amount. Reproduced from Yu et al. (2014) with permission from the American Chemical Society.

with graphene is also an efficient strategy to enhance the activity of anatase $TiO_2$ facet heterojunction ({101}/{001}) for the photoreduction of $CO_2$ (Xiong et al., 2016). Charge transfer between {101} and {001} facets along with the migration of electrons from $TiO_2$ to graphene greatly improved the separation efficiency of photogenerated carriers, thus increasing the yield of CO by photoreducing $CO_2$. Photocatalytic $CO_2$ reduction performance of the typical $TiO_2$-based phase or facet heterojunctions above are listed in **Table 3**.

## CONCLUSIONS AND PROSPECTS

This review summarizes the recent advances in the rational design, fabrication and photocatalytic performance of $TiO_2$-based heterojunctions for converting $CO_2$ into solar fuels with water oxidation. Generally, photocatalytic $CO_2$ reduction that mimic the nature photosynthesis of green plants exhibits great potential for the reduction of $CO_2$ level in the atmosphere and storage of solar energy in hydrocarbon fuels, so as to alleviate the impact of energy crisis and climate change on the development of human society. However, some obstacles, such as low solar energy conversion efficiency, slow generation rate and poor selectivity toward reduction products of $CO_2$, and common photocorrosion phenomenon facing the current photocatalytic systems, restricts the practical application of this very promising technology. In recent years, tremendous efforts have been devoted to fabricate $TiO_2$-based heterojunctions, in order to realize enhanced photocatalytic performance for $CO_2$ conversion, thus giving new life to this traditional and systematically studied photocatalyst. Although the composition, morphology, architecture and photocatalytic mechanism of $TiO_2$-based heterojunctions are various, they have much in common that favors for photoreduction of $CO_2$ as follows: 1) the efficient electron transfer at the heterointerface that promotes spatial separation of photogenerated $e^-/h^+$ pairs and prolongs their lifetime to participate in the photoinduced redox reactions; 2) the expanded light adsorption range and enhanced visible light responsibility, making it possible for solar-driven photocatalytic $CO_2$ reduction; 3) the enlarged $CO_2$ adsorption capacity due to the high specific surface area with highly exposed active sites that combine $CO_2$ by chemical action, which could also activate the adsorbed $CO_2$ molecules and facilitate hydrocarbon generation; 4) the increase in selectivity toward specific photoreduction products of $CO_2$ is attributed to the contribution of the cocatalysts.

Although considerable progress has been made on $TiO_2$-based heterojunction for photocatalytic $CO_2$ reduction, it is still far from practical application. On the one hand, the formation of multi-carbon products has always been a bottleneck in this field. The study of $CO_2$ photoreduction intermediates combined with *in-situ* analysis technology and theoretical calculations needs to be more in-depth in order to clarify the formation mechanisms of different hydrocarbons and guide for the rational design of photocatalysts for the generation of multi-carbon product with high selectivity. On the other hand, pre-defined design of the components and their spatial arrangement in the heterojunction for the optimized phtotcatalytic performance is still a great challenge. It is worth nothing that the difference in synthesis conditions limits the flexibility of component selection, which also complicates the synthesis procedure and reduces the yield of expected heterojunction photocatalyst. At the same time, the randomness arrangement of different components in many cases and the variability of the catalyst morphology and structure affect the photocatalytic performance significantly, which also makes it difficult to clarify the contribution of each component and the synergism mechanism. How to overcome the above limitations to select components of the heterojunction based on photocatalytic performance only, and achieve precise control at the structural unit level, thus realizing efficient synergy of each component for

photocatalytic $CO_2$ reduction is one of the main directions of future development in this field. To our knowledge, recent advances in DNA origami superlattice structure (Tian et al., 2016; Tian et al., 2020) may provide a possible solution and guide the design and construction of well-ordered heterojunction photocatalysts in the future. Specifically, the precisely control of the topological structure, arrangement sequence, and assembly quantity of each building block (polyhedral DNA frame) during the self-assembly process makes it possible for heterojunction photocatalysts with controllable structure and adjustable performance, which is expected to become the future research hotspot in the field of photocatalytic $CO_2$ reduction. In addition, efficient solar harvesting systems are in great demand to replace artificial light sources with high energy consumption, since efficient photoreduction of $CO_2$ is based on high light intensity. On the one hand, upconversion quantum dots can be introduced into the heterostructured photocatalyst, in which some of the long-waved visible light in the incident light can be converted into short-waved partial that can excite the photocatalyst to generate $e^-$ and $h^+$ pairs. On the other hand, focusing lens system can be added to the photoreactor to enhance the concentration of sunlight, then the photocatalyst can operate under higher light intensity and exhibit optimized activity. Although the efficiency of photocatalytic $CO_2$ reduction is far less than that of electrocatalysis, relying entirely on solar energy will become its irreplaceable advantage. Furthermore, the enrichment of $CO_2$ in air will become an important consideration in the design of heterojunction photocatalysts, which meet the needs of practical applications. Fortunately, the research on $CO_2$ storage and controlled release provides the possible solution while the visible light-triggered capture and release of $CO_2$ from stable MOFs become the most promising candidate (Park et al., 2011; Li et al., 2016; Lyndon et al., 2015). Obviously, combination of photocatalyst and the above MOFs can realize the efficient recycling of $CO_2$ and improve the efficiency of its conversion into solar fuel, which is expected to become a research hot spot in the future.

In summary, the heterojunction photocatalysts with well-organized structure, optimized solar energy conversion efficiency, ideal turnover frequency of $CO_2$, and high reduction product selectivity are still the direction of efforts in the future. We hope that this review can inspire new ideas to guide the design and synthesis of high-performance photocatalysts for photoreduction of $CO_2$ into solar fuels, thus accelerating the industrialization process of this very promising technology and providing practical help to alleviate energy and environmental crises.

## AUTHOR CONTRIBUTIONS

KL designed and wrote the review with input from CT, YT, SW, and QM for conceiving, writing, and editing the manuscript.

## FUNDING

This study was supported by Shenzhen Science and Technology Innovation Program (Grand No. GJHZ20190819151807167), Post-doctoral Foundation Project of Shenzhen Polytechnic (Grand No. 6020330008K0), the Fundamental Research Funds for the Central Universities (Grand No. 020514380141), and China Postdoctoral Science Foundation (Grand No. 2020M671437).

## REFERENCES

Aguirre, M. E., Zhou, R., Eugene, A. J., Guzman, M. I., and Grela, M. A. (2017). $Cu_2O/TiO_2$ heterostructures for $CO_2$ reduction through a direct Z-scheme: protecting $Cu_2O$ from photocorrosion. *Appl. Catal. B* 217, 485–493. doi:10.1016/j.apcatb.2017.05.058

An, X., Li, K., and Tang, J. (2014). $Cu_2O$/reduced graphene oxide composites for the photocatalytic conversion of $CO_2$. *ChemSusChem* 7 (4), 1086–1093. doi:10.1002/cssc.201301194

Aresta, M., Dibenedetto, A., and Angelini, A. (2014). Catalysis for the valorization of exhaust carbon: from $CO_2$ to chemicals, materials, and fuels. Technological use of $CO_2$. *Chem. Rev.* 114 (3), 1709–1742. doi:10.1021/cr4002758

Bai, S., Jiang, J., Zhang, Q., and Xiong, Y. (2015). Steering charge kinetics in photocatalysis: intersection of materials syntheses, characterization techniques and theoretical simulations. *Chem. Soc. Rev.* 44, 2893–2939. doi:10.1039/c5cs00064e

Barber, J. (2009). Photosynthetic energy conversion: natural and artificial. *Chem. Soc. Rev.* 38 (1), 185–196. doi:10.1039/b802262n

Bie, C., Zhu, B., Xu, F., Zhang, L., and Yu, J. (2019). *In situ* grown monolayer N-doped graphene on CdS hollow spheres with seamless contact for photocatalytic $CO_2$ reduction. *Adv. Mater.* 31 (42), 1902868. doi:10.1002/adma.201902868

Biswas, M. R. U. D., Ali, A., Cho, K. Y., and amd Oh, W. C. (2018). Novel synthesis of $WSe_2$ -graphene-$TiO_2$ ternary nanocomposite *via* ultrasonic technics for high photocatalytic reduction of $CO_2$ into $CH_3OH$. *Ultrason. Sonochem.* 42, 738–746. doi:10.1016/j.ultsonch.2017.12.030

Brockway, P. E., Owen, A., Brand-Correa, L. I., and Hardt, L. (2019). Estimation of global final-stage energy-return-on-investment for fossil fuels with comparison to renewable energy sources. *Nat. Energ.* 4 (7), 612–621. doi:10.1038/s41560-019-0425-z

Cao, S., Shen, B., Tong, T., Fu, J., and Yu, J. (2018). 2D/2D heterojunction of ultrathin MXene/$Bi_2WO_6$ nanosheets for improved photocatalytic $CO_2$ reduction. *Adv. Funct. Mater.* 28 (21), 1800136. doi:10.1002/adfm.201800136

Cao, Y., Li, Q., Li, C., Li, J., and Yang, J. (2016). Surface heterojunction between (001) and (101) facets of ultrafine anatase $TiO_2$ nanocrystals for highly efficient photoreduction $CO_2$ to $CH_4$. *Appl. Catal. B* 198, 378–388. doi:10.1016/j.apcatb.2016.05.071

Chen, S., Gao, H., Han, M., Chen, X., Zhang, X., Dong, W., et al. (2020). *In situ* self-transformation synthesis of N-doped carbon coating paragenetic anatase/rutile heterostructure with enhanced photocatalytic $CO_2$ reduction activity. *ChemCatChem* 12, 3274–3284. doi:10.1002/cctc.202000137

Chen, X., Zhou, Y., Liu, Q., Li, Z., Liu, J., and Zou, Z. (2012). Ultrathin, single-crystal $WO_3$ nanosheets by two-dimensional oriented attachment toward enhanced photocatalystic reduction of $CO_2$ into hydrocarbon fuels under visible light. *ACS Appl. Mater. Inter.* 4 (7), 3372–3377. doi:10.1021/am300661s

Cheng, X., Dong, P., Huang, Z., Zhang, Y., Chen, Y., Nie, X., et al. (2017). Green synthesis of plasmonic Ag nanoparticles anchored $TiO_2$ nanorod arrays using cold plasma for visible-light-driven photocatalytic reduction of $CO_2$. *J. Co$_2$* Util. 20, 200–207. doi:10.1016/j.jcou.2017.04.009

Chong, R., Su, C., Du, Y., Fan, Y., Ling, Z., Chang, Z., et al. (2018). Insights into the role of MgAl layered double oxides interlayer in Pt/$TiO_2$ toward photocatalytic $CO_2$ reduction. *J. Catal.* 363, 92–101. doi:10.1016/j.jcat.2018.04.020

Chowdhury, S., Parshetti, G. K., and Balasubramanian, R. (2015). Post-combustion $CO_2$ capture using mesoporous $TiO_2$/graphene oxide nanocomposites. *Chem. Eng. J.* 263, 374–384. doi:10.1016/j.cej.2014.11.037

Corma, A., and Garcia, H. (2013). Photocatalytic reduction of $CO_2$ for fuel production: possibilities and challenges. *J. Catal.* 308, 168–175. doi:10.1016/j.jcat.2013.06.008

Di Liberto, G., Tosoni, S., and Pacchioni, G. (2019). Role of heterojunction in charge carriers separation in coexposed anatase (001)-(101) surfaces. *J. Phys. Chem. Lett.* 10, 2372–2377. doi:10.1021/acs.jpclett.9b00504

Dogutan, D. K., and Nocera, D. G. (2019). Artificial photosynthesis at efficiencies greatly exceeding that of natural photosynthesis. *Acc. Chem. Res.* 52 (11), 3143–3148. doi:10.1021/acs.accounts.9b00380

Fu, J., Jiang, K., Qiu, X., Yu, J., and Liu, M. (2019). Product selectivity of photocatalytic CO2 reduction reactions. *Mater. Today* 32, 222–243. doi:10.1016/j.mattod.2019.06.009

Fujishima, A., and Honda, K. (1972). Electrochemical photolysis of water at a semiconductor electrode. *Nature* 238 (5358), 37–38. doi:10.1038/238037a0

Ganesh, I. (2014). Conversion of carbon dioxide into methanol-a potential liquid fuel: fundamental challenges and opportunities (a review). *Renew. Sustain. Energ. Rev* 31, 221–257. doi:10.1016/j.rser.2013.11.045

Gui, M. M., Chai, S. P., Xu, B. Q., and Mohamed, A. R. (2014). Enhanced visible light responsive MWCNT/$TiO_2$ core–shell nanocomposites as the potential photocatalyst for reduction of $CO_2$ into methane. *Sol. Energ. Mater. Sol. Cell* 122, 183–189. doi:10.1016/j.solmat.2013.11.034

Gui, M. M., Wong, W. M. P., Chai, S. P., and Mohamed, A. R. (2015). One-pot synthesis of Ag-MWCNT@$TiO_2$ core-shell nanocomposites for photocatalytic reduction of $CO_2$ with water under visible light irradiation. *Chem. Eng. J.* 278, 272–278. doi:10.1016/j.cej.2014.09.022

Habisreutinger, S. N., Schmidt-Mende, L., and Stolarczyk, J. K. (2013). Photocatalytic reduction of $CO_2$ on $TiO_2$ and other semiconductors. *Angew. Chem. Int. Ed.* 52 (29), 7372–7408. doi:10.1002/anie.201207199

He, Y., Zhang, L., Fan, M., Wang, X., Walbridge, M. L., Nong, Q., et al. (2015). Z-scheme $SnO_{2-x}$/g-$C_3N_4$ composite as an efficient photocatalyst for dye degradation and photocatalytic $CO_2$ reduction. *Sol. Energ. Mater. Sol. Cell* 137, 175–184. doi:10.1016/j.solmat.2015.01.037

Höök, M., and Tang, X. (2013). Depletion of fossil fuels and anthropogenic climate change-A review. *Energy Policy* 52, 797–809. doi:10.1016/j.enpol.2012.10.046

Hwang, H. M., Oh, S., Shim, J. H., Kim, Y. M., Kim, A., Kim, D., et al. (2019). Phase-selective disordered anatase/ordered rutile interface system for visible-light-driven, metal-free $CO_2$ reduction. *ACS Appl. Mater. Inter.* 11, 35693–35701. doi:10.1021/acsami.9b10837

Inoue, T., Fujishima, A., Konishi, S., and Honda, K. (1979). Photoelectrocatalytic reduction of carbon dioxide in aqueous suspensions of semiconductor powders. *Nature* 277 (5698), 637–638. doi:10.1038/277637a0

Iqbal, F., Mumtaz, A., Shahabuddin, S., Abd Mutalib, M. I., Shaharun, M. S., Nguyen, T. D., et al. (2020). Photocatalytic reduction of $CO_2$ to methanol over $ZnFe_2O_4$/$TiO_2$ (p-n) heterojunctions under visible light irradiation. *J. Chem. Technol. Biot.* 95 (8), 2208–2221. doi:10.1002/jctb.6408

Jiao, J., Wei, Y., Zhao, Z., Zhong, W., Liu, J., Li, J., et al. (2015). Synthesis of 3D ordered macroporous $TiO_2$-supported Au nanoparticle photocatalysts and their photocatalytic performances for the reduction of $CO_2$ to methane. *Catal. Today* 258, 319–326. doi:10.1016/j.cattod.2015.01.030

Jin, J., Chen, S., Wang, J., Chen, C., and Peng, T. (2019). $SrCO_3$-modified brookite/anatase $TiO_2$ heterophase junctions with enhanced activity and selectivity of $CO_2$ photoreduction to $CH_4$. *Appl. Surf. Sci.* 476, 937–947. doi:10.1016/j.apsusc.2019.01.176

Jung, H., Cho, K. M., Kim, K. H., Yoo, H. W., Al-Saggaf, A., Gereige, I., et al. (2018). Highly efficient and stable $CO_2$ reduction photocatalyst with a hierarchical structure of mesoporous $TiO_2$ on 3D graphene with few-layered $MoS_2$. *ACS Sustain. Chem. Eng.* 6 (5), 5718–5724. doi:10.1021/acssuschemeng.8b00002

Kegel, J., Povey, I. M., and Pemble, M. E. (2018). Zinc oxide for solar water splitting: a brief review of the material's challenges and associated opportunities. *Nano Energy* 54, 409–428. doi:10.1016/j.nanoen.2018.10.043

Khatun, F., Abd Aziz, A., Sim, L. C., and Monir, M. U. (2019). Plasmonic enhanced Au decorated $TiO_2$ nanotube arrays as a visible light active catalyst towards photocatalytic $CO_2$ conversion to $CH_4$. *J. Environ. Chem. Eng.* 7, 103233. doi:10.1016/j.jece.2019.103233

Kim, K. H., Kim, S., Moon, B. C., Choi, J. W., Jeong, H. M., Kwon, Y., et al. (2017). Quadruple metal-based layered structure as the photocatalyst for conversion of carbon dioxide into a value added carbon monoxide with high selectivity and efficiency. *J. Mater. Chem. A.* 5 (18), 8274–8279. doi:10.1039/c7ta01623a

Kondratenko, E. V., Mul, G., Baltrusaitis, J., Larrazabal, G. O., and Perez-Ramirez, J. (2013). Status and perspectives of $CO_2$ conversion into fuels and chemicals by catalytic, photocatalytic and electrocatalytic processes. *Energy Environ. Sci.* 6 (11), 3112–3135. doi:10.1039/c3ee41272e

Kuai, L., Zhou, Y., Tu, W., Li, P., Li, H., Xu, Q., et al. (2015). Rational construction of a CdS/reduced graphene oxide/$TiO_2$ core-shell nanostructure as an all-solid-state Z-scheme system for $CO_2$ photoreduction into solar fuels. *RSC Adv.* 5 (107), 88409–88413. doi:10.1039/c5ra14374h

Kuehnel, M. F., Orchard, K. L., Dalle, K. E., and Reisner, E. (2017). Selective photocatalytic $CO_2$ reduction in water through anchoring of a molecular Ni catalyst on CdS nanocrystals. *J. Am. Chem. Soc.* 139 (21), 7217–7223. doi:10.1021/jacs.7b00369

Lee, J. D., Sorescu, C., and Deng, X. Y. (2011). Electron-induced dissociation of $CO_2$ on $TiO_2$(110). *J. Am. Chem. Soc.* 133 (26), 10066–10069. doi:10.1021/ja204077e

Lee, J. S., Won, D. I., Jung, W. J., Son, H. J., Pac, C., and Kang, S. O. (2016). Widely controllable syngas production by a dye-sensitized $TiO_2$ hybrid system with $Re^{I}$ and $Co^{III}$ catalysts under visible-light irradiation. *Angew. Chem. Int. Ed.* 56 (4), 976–980. doi:10.1002/anie.201608593

Lee, K. M., Lai, C. W., Ngai, K. S., and Juan, J. C. (2016). Recent developments of zinc oxide based photocatalyst in water treatment technology: a review. *Water Res.* 88, 428–448. doi:10.1016/j.watres.2015.09.045

Lee, K. Y., Sato, K., and Mohamed, A. R. (2016). Facile synthesis of anatase-rutile $TiO_2$ composites with enhanced $CO_2$ photoreduction activity and the effect of Pt loading on product selectivity. *Mater. Lett.* 163, 240–243. doi:10.1016/j.matlet.2015.10.094

Lee, J. H., Kim, S. I., Park, S. M., and Kang, M. (2017). A p-n heterojunction NiS-sensitized $TiO_2$ photocatalytic system for efficient photoreduction of carbon dioxide to methane. *Ceram. Int.* 43 (2), 1768–1774. doi:10.1016/j.ceramint.2016.10.122

Li, H., Sadiq, M. M., Suzuki, K., Ricco, R., Doblin, C., Hill, A. J., et al. (2016). Magnetic metal-organic frameworks for efficient carbon dioxide capture and remote trigger release. *Adv. Mater.* 28 (9), 1839–1844. doi:10.1002/adma.201505320

Li, M., Wang, M., Zhu, L., Li, Y., Yan, Z., Shen, Z., et al. (2018). Facile microwave assisted synthesis of N-rich carbon quantum dots/dual-phase $TiO_2$ heterostructured nanocomposites with high activity in $CO_2$ photoreduction. *Appl. Catal. B* 231, 269–276. doi:10.1016/j.apcatb.2018.03.027

Li, X., Yu, J., Jaroniec, M., and Chen, X. (2019). Cocatalysts for selective photoreduction of $CO_2$ into solar fuels. *Chem. Rev.* 119, 3962–4179. doi:10.1021/acs.chemrev.8b00400

Lin, L. Y., Nie, Y., Kavadiya, S., Soundappan, T., and Biswas, P. (2017). N-doped reduced graphene oxide promoted nano $TiO_2$ as a bifunctional adsorbent/photocatalyst for $CO_2$ photoreduction: effect of N species. *Chem. Eng. J.* 316, 449–460. doi:10.1016/j.cej.2017.01.125

Liu, L., Jiang, Y., Zhao, H., Chen, J., Cheng, J., Yang, K., et al. (2016). Engineering coexposed {001} and {101} facets in oxygen-deficient $TiO_2$ nanocrystals for enhanced $CO_2$ photoreduction under visible light. *ACS Catal.* 6 (2), 1097–1108. doi:10.1021/acscatal.5b02098

Liu, X., Inagaki, S., and Gong, J. (2016). Heterogeneous molecular systems for photocatalytic $CO_2$ reduction with water oxidation. *Angew. Chem. Int. Ed.* 55 (48), 14924–14950. doi:10.1002/anie.201600395

Liu, Y., Shen, D., Zhang, Q., Lin, Y., and Peng, F. (2021). Enhanced photocatalytic $CO_2$ reduction in $H_2O$ vapor by atomically thin $Bi_2WO_6$ nanosheets with hydrophobic and nonpolar surface. *Appl. Catal. B* 283, 119630. doi:10.1016/j.apcatb.2020.119630

Low, J., Qiu, S., Xu, D., Jiang, C., and Cheng, B. (2018). Direct evidence and enhancement of surface plasmon resonance effect on Ag-loaded $TiO_2$ nanotube arrays for photocatalytic $CO_2$ reduction. *Appl. Surf. Sci.* 434, 423–432. doi:10.1016/j.apsusc.2017.10.194

Low, J., Dai, B., Tong, T., Jiang, C., and Yu, J. (2019). *In situ* irradiated X-ray photoelectron spectroscopy investigation on a direct Z-scheme $TiO_2$/CdS composite film photocatalyst. *Adv. Mater.* 31, 1802981. doi:10.1002/adma.201802981

Lyndon, R., Konstas, K., Thornton, A. W., Seeber, A. J., Ladewig, B. P., and Hill, M. R. (2015). Visible light-triggered capture and release of CO2 from stable metal

organic frameworks. *Chem. Mater.* 27 (23), 7882–7888. doi:10.1021/acs.chemmater.5b02211

Ma, Y., Wang, X., Jia, Y., Chen, X., Han, H., and Li, C. (2014). Titanium dioxide-based nanomaterials for photocatalytic fuel generations. *Chem. Rev.* 114 (19), 9987–10043. doi:10.1021/cr500008u

Mao, J., Peng, T., Zhang, X., Li, K., and Zan, L. (2012). Selective methanol production from photocatalytic reduction of $CO_2$ on $BiVO_4$ under visible light irradiation. *Catal. Commun.* 28, 38–41. doi:10.1016/j.catcom.2012.08.008

Meinshausen, M., Meinshausen, N., Hare, W., Raper, S. C. B., Frieler, K., Knutti, R., et al. (2009). Greenhouse-gas emission targets for limiting global warming to 2 °C. *Nature* 458 (7242), 1158–1162. doi:10.1038/nature08017

Meng, A., Zhang, L., Cheng, B., and Yu, J. (2019). $TiO_2$-$MnO_x$-Pt hybrid multiheterojunction film photocatalyst with enhanced photocatalytic $CO_2$-reduction activity. *ACS Appl. Mater. Inter.* 11, 5581–5589. doi:10.1021/acsami.8b02552

Neaţu, Ş., Maciá-Agulló, J. A., Concepción, P., and Garcia, H. (2014). Gold-copper nanoalloys supported on $TiO_2$ as photocatalysts for $CO_2$ reduction by water. *J. Am. Chem. Soc.* 136 (45), 15969–15976. doi:10.1021/ja506433k

Nguyen, T. P., Nguyen, D. L. T., Nguyen, V. H., Le, T. H., Vo, D. V. N., Trinh, Q. T., et al. (2020). Recent advances in $TiO_2$-based photocatalysts for reduction of $CO_2$ to fuels. *Nanomaterials* 10 (2), 337. doi:10.3390/nano10020337

Nie, N., Zhang, L., Fu, J., Cheng, B., and Yu, J. (2018). Self-assembled hierarchical direct Z-scheme g-$C_3N_4$/ZnO microspheres with enhanced photocatalytic $CO_2$ reduction performance. *Appl. Surf. Sci.* 441, 12–22. doi:10.1016/j.apsusc.2018.01.193

Ola, O., and Maroto-Valer, M. M. (2015). Review of material design and reactor engineering on $TiO_2$ photocatalysis for $CO_2$ reduction. *J. Photochem. Photobiol. C* 24, 16–42. doi:10.1016/j.jphotochemrev.2015.06.001

Olah, G. A., Prakash, G. K. S., and Goeppert, A. (2011). Anthropogenic chemical carbon cycle for a sustainable future. *J. Am. Chem. Soc.* 133 (33), 12881–12898. doi:10.1021/ja202642y

Olowoyo, J. O., Kumar, M., Jain, S. L., Babalola, J. O., Vorontsov, A. V., and Kumar, U. (2018). Insight into reinforced photocatalytic activity of CNT-$TiO_2$ nanocomposite for $CO_2$ reduction and water splitting. *J. Phys. Chem. C* 123, 367–378. doi:10.1021/acs.jpcc.8b07894

Olowoyo, J. O., Kumar, M., Singh, B., Oninla, V. O., Babalola, J. O., Valdés, H., et al. (2019). Self-assembled reduced graphene oxide-$TiO_2$ nanocomposites: synthesis, DFTB+ calculations, and enhanced photocatalytic reduction of $CO_2$ to methanol. *Carbon* 147, 385–397. doi:10.1016/j.carbon.2019.03.019

Park, J., Yuan, D., Pham, K. T., Li, J. R., Yakovenko, A., and Zhou, H. C. (2011). Reversible alteration of CO2 adsorption upon photochemical or thermal treatment in a metal-organic framework. *J. Am. Chem. Soc.* 134 (1), 99–102. doi:10.1021/ja209197f

Patil, S. B., Basavarajappa, P. S., Ganganagappa, N., Jyothi, M. S., Raghu, A. V., and Reddy, K. R. (2019). Recent advances in non-metals-doped $TiO_2$ nanostructured photocatalysts for visible-light driven hydrogen production, $CO_2$ reduction and air purification. *Inter. J. Hydrogen Energ.* doi:10.1016/j.ijhydene.2019.03.164

Raza, A., Shen, H., Haidry, A. A., Sun, L., Liu, R., and Cui, S. (2020). Studies of Z-scheme $WO_3$-$TiO_2$/$Cu_2ZnSnS_4$ ternary nanocomposite with enhanced $CO_2$ photoreduction under visible light irradiation. *J. Co$_2$* Util. 37, 260–271. doi:10.1016/j.jcou.2019.12.020

Reñones, P., Moya, A., Fresno, F., Collado, L., Vilatela, J. J., and de la Peña O'Shea, V. A. (2016). Hierarchical $TiO_2$ nanofibres as photocatalyst for $CO_2$ reduction: influence of morphology and phase composition on catalytic activity. *J. Co$_2$* Util. 15, 24–31. doi:10.1016/j.jcou.2016.04.002

Rodríguez, V., Camarillo, R., Martínez, F., Jiménez, C., and Rincón, J. (2020). $CO_2$ photocatalytic reduction with CNT/$TiO_2$ based nanocomposites prepared by high-pressure technology. *J. Supercrit. Fluids* 163, 104876. doi:10.1016/j.supflu.2020.104876

She, H., Wang, Y., Zhou, H., Li, Y., Wang, L., Huang, J., et al. (2018). Preparation of $Zn_3In_2S_6$/$TiO_2$ for enhanced $CO_2$ photocatalytic reduction activity *via* Z-scheme electron transfer. *ChemCatChem* 11, 753–759. doi:10.1002/cctc.201801745

Shehzad, N., Tahir, M., Johari, K., Murugesan, T., and Hussain, M. (2018a). Improved interfacial bonding of graphene-$TiO_2$ with enhanced photocatalytic reduction of $CO_2$ into solar fuel. *J. Environ. Chem. Eng.* 6, 6947–6957. doi:10.1016/j.jece.2018.10.065

Shehzad, N., Tahir, M., Johari, K., Murugesan, T., and Hussain, M. (2018b). A critical review on $TiO_2$ based photocatalytic $CO_2$ reduction system: strategies to improve efficiency. *J. Co$_2$ Util.* 26, 98–122. doi:10.1016/j.jcou.2018.04.026

Shi, W., Guo, X., Cui, C., Jiang, K., Li, Z., Qu, L., et al. (2019). Controllable synthesis of $Cu_2O$ decorated $WO_3$ nanosheets with dominant (001) facets for photocatalytic $CO_2$ reduction under visible-light irradiation. *Appl. Catal. B* 243, 236–242. doi:10.1016/j.apcatb.2018.09.076

Shindell, D., and Smith, C. J. (2019). Climate and air-quality benefits of a realistic phase-out of fossil fuels. *Nature* 573 (7774), 408–411. doi:10.1038/s41586-019-1554-z

Sim, L. C., Leong, K. H., Saravanan, P., and Ibrahim, S. (2015). Rapid thermal reduced graphene oxide/Pt-$TiO_2$ nanotube arrays for enhanced visible-light-driven photocatalytic reduction of $CO_2$. *Appl. Surf. Sci.* 358, 122–129. doi:10.1016/j.apsusc.2015.08.065

Solomon, S., Plattner, G. K., Knutti, R., and Friedlingstein, P. (2009). Irreversible climate change due to carbon dioxide emissions. *Proc. Natl. Acad. Sci. U. S. A.* 106, 1704–1709. doi:10.1073/pnas.0812721106

Stott, P. A., Tett, S., Jones, G., Allen, M., Mitchell, J., and Jenkins, G. (2000). External control of 20th century temperature by natural and anthropogenic forcings. *Science* 290 (5499), 2133–2137. doi:10.1126/science.290.5499.2133

Tahir, M., Tahir, B., and Amin, N. A. S. (2017). Synergistic effect in plasmonic Au/Ag alloy NPs co-coated $TiO_2$ NWs toward visible-light enhanced $CO_2$ photoreduction to fuels. *Appl. Catal. B* 204, 548–560. doi:10.1016/j.apcatb.2016.11.062

Tahir, M. (2020). Well-designed $ZnFe_2O_4$/Ag/$TiO_2$ nanorods heterojunction with Ag as electron mediator for photocatalytic $CO_2$ reduction to fuels under UV/visible light. *J. Co$_2$* Util. 37, 134–146. doi:10.1016/j.jcou.2019.12.004

Takayama, T., Sato, K., Fujimura, T., Kojima, Y., Iwase, A., and Kudo, A. (2017). Photocatalytic $CO_2$ reduction using water as an electron donor by a powdered Z-scheme system consisting of metal sulfide and an RGO-$TiO_2$ composite. *Faraday Discuss.* 198, 397–407. doi:10.1039/c6fd00215c

Tan, L. L., Ong, W. J., Chai, S. P., and Mohamed, A. R. (2015). Noble metal modified reduced graphene oxide/$TiO_2$ ternary nanostructures for efficient visible-light-driven photoreduction of carbon dioxide into methane. *Appl. Catal. B* 166-167, 251–259. doi:10.1016/j.apcatb.2014.11.035

Tan, L. L., Ong, W. J., Chai, S. P., and Mohamed, A. R. (2017). Photocatalytic reduction of $CO_2$ with $H_2O$ over graphene oxide-supported oxygen-rich $TiO_2$ hybrid photocatalyst under visible light irradiation: process and kinetic studies. *Chem. Eng. J.* 308, 248–255. doi:10.1016/j.cej.2016.09.050

Tan, D., Zhang, J., Shi, J., Li, S., Zhang, B., Tan, X., et al. (2018). Photocatalytic $CO_2$ transformation to $CH_4$ by Ag/Pd bimetals supported on N-doped $TiO_2$ nanosheet. *ACS Appl. Mater. Inter.* 10 (29), 24516–24522. doi:10.1021/acsami.8b06320

Tasbihi, M., Fresno, F., Simon, U., Villar-García, I. J., Pérez-Dieste, V., Escudero, C., et al. (2018a). On the selectivity of $CO_2$ photoreduction towards $CH_4$ using Pt/$TiO_2$ catalysts supported on mesoporous silica. *Appl. Catal. B* 239, 68–76. doi:10.1016/j.apcatb.2018.08.003

Tasbihi, M., Kočí, K., Edelmannová, M., Troppová, I., Reli, M., and Schomäcker, R. (2018b). Pt/$TiO_2$ photocatalysts deposited on commercial support for photocatalytic reduction of $CO_2$. *J. Photochem. Photobiol. A.* 366, 72–80. doi:10.1016/j.jphotochem.2018.04.012

Thi Thanh Truc, N., Giang Bach, L., Thi Hanh, N., Pham, T. D., Thi Phuong Le Chi, N., Trinh Tran, D., et al. (2019). The superior photocatalytic activity of Nb doped $TiO_2$/g-$C_3N_4$ direct Z-scheme system for efficient conversion of $CO_2$ into valuable fuels. *J. Colloid Interf. Sci.* 540, 1–8. doi:10.1016/j.jcis.2019.01.005

Tian, Y., Lhermitte, J. R., Bai, L., Vo, T., Xin, H. L., Li, H., et al. (2020). Ordered three-dimensional nanomaterials using DNA-prescribed and valence-controlled material voxels. *Nat. Mater.* doi:10.1038/s41563-019-0550-x

Tian, Y., Zhang, Y., Wang, T., Xin, H. L., Li, H., and Gang, O. (2016). Lattice engineering through nanoparticle-DNA frameworks. *Nat. Mater.* 15, 654–661. doi:10.1038/NMAT4571

Tu, W., Zhou, Y., Liu, Q., Yan, S., Bao, S., Wang, X., et al. (2013). An *in situ* simultaneous reduction-hydrolysis technique for fabrication of $TiO_2$-graphene 2D sandwich-like hybrid nanosheets: graphene-promoted selectivity of photocatalytic-driven hydrogenation and coupling of $CO_2$ into methane and ethane. *Adv. Funct. Mater.* 23 (14), 1743–1749. doi:10.1002/adfm.201202349

Tu, W., Zhou, Y., and Zou, Z. (2014). Photocatalytic conversion of $CO_2$ into renewable hydrocarbon fuels: state-of-the-art accomplishment, challenges, and prospects. *Adv. Mater.* 26 (27), 4607–4626. doi:10.1002/adma.201400087

Tu, W., Guo, W., Hu, J., He, H., Li, H., Li, Z., et al. (2020). State-of-the-art advancements of crystal facet-exposed photocatalysts beyond $TiO_2$: design and dependent performance for solar energy conversion and environment applications. *Mater. Today* 33, 75–86. doi:10.1016/j.mattod.2019.09.003

Wang, H., Zhang, L., Chen, Z., Hu, J., Li, S., Wang, Z., et al. (2014). Semiconductor heterojunction photocatalysts: design, construction, and photocatalytic performances. *Chem. Soc. Rev.* 43 (15), 5234. doi:10.1039/c4cs00126e

Wang, W., Xu, D., Cheng, B., Yu, J., and Jiang, C. (2017). Hybrid carbon@$TiO_2$ hollow spheres with enhanced photocatalytic $CO_2$ reduction activity. *J. Mater. Chem. A.* 5 (10), 5020–5029. doi:10.1039/c6ta11121a

Wang, H., Yong, D., Chen, S., Jiang, S., Zhang, X., Shao, W., et al. (2018). Oxygen-vacancy-mediated exciton dissociation in BiOBr for boosting charge-carrier-involved molecular oxygen activation. *J. Am. Chem. Soc.* 140 (5), 1760–1766. doi:10.1021/jacs.7b10997

Wang, H., Zhang, L., Wang, K., Sun, X., and Wang, W. (2019). Enhanced photocatalytic $CO_2$ reduction to methane over $WO_3{\cdot}0.33H_2O$ *via* Mo doping. *Appl. Catal. B* 243, 771–779. doi:10.1016/j.apcatb.2018.11.021

Wang, K., Jiang, R., Peng, T., Chen, X., Dai, W., and Fu, X. (2019). Modeling the effect of Cu doped $TiO_2$ with carbon dots on $CO_2$ methanation by $H_2O$ in a photo-thermal system. *Appl. Catal. B* 256, 117780. doi:10.1016/j.apcatb.2019.117780

Wang, L., Jin, P., Huang, J., She, H., and Wang, Q. (2019). Integration of copper(II)-porphyrin zirconium metal-organic framework and titanium dioxide to construct Z-scheme system for highly improved photocatalytic $CO_2$ reduction. *ACS Sustain. Chem. Eng.* 7, 15660–15670. doi:10.1021/acssuschemeng.9b03773

Wang, R., Shen, J., Sun, K., Tang, H., and Liu, Q. (2019). Enhancement in photocatalytic activity of $CO_2$ reduction to $CH_4$ by 0D/2D Au/$TiO_2$ plasmon heterojunction. *Appl. Surf. Sci.* 493, 1142–1149. doi:10.1016/j.apsusc.2019.07.121

Wang, C., Liu, X., He, W., Zhao, Y., Wei, Y., Xiong, J., et al. (2020a). All-solid-state Z-scheme photocatalysts of g-$C_3N_4$/Pt/macroporous-($TiO_2$@carbon) for selective boosting visible-light-driven conversion of $CO_2$ to $CH_4$. *J. Catal.* 389, 440–449. doi:10.1016/j.jcat.2020.06.026

Wang, C., Zhao, Y., Xu, H., Li, Y., Wei, Y., Liu, J., et al. (2020b). Efficient Z-scheme photocatalysts of ultrathin g-$C_3N_4$-wrapped Au/$TiO_2$-nanocrystals for enhanced visible-light-driven conversion of $CO_2$ with $H_2O$. *Appl. Catal. B* 263, 118314. doi:10.1016/j.apcatb.2019.118314

Wang, A., Wu, S., Dong, J., Wang, R., Wang, J., Zhang, J., et al. (2021). Interfacial facet engineering on the Schottky barrier between plasmonic Au and $TiO_2$ in boosting the photocatalytic $CO_2$ reduction under ultraviolet and visible light irradiation. *Chem. Eng. J.* 404, 127145. doi:10.1016/j.cej.2020.127145

Wei, L., Yu, C., Zhang, Q., Liu, H., and Wang, Y. (2018). $TiO_2$-based heterojunction photocatalysts for photocatalytic reduction of $CO_2$ to solar fuels. *J. Mater. Chem. A.* 6, 22411–22436. doi:10.1039/c8ta08879a

Wei, Y., Wu, X., Zhao, Y., Wang, L., Zhao, Z., Huang, X., et al. (2018). Efficient photocatalysts of $TiO_2$ nanocrystals-supported PtRu alloy nanoparticles for $CO_2$ reduction with $H_2O$: synergistic effect of Pt-Ru. *Appl. Catal. B* 236, 445–457. doi:10.1016/j.apcatb.2018.05.043

Wei, Z. H., Wang, Y. F., Li, Y. Y., Zhang, L., Yao, H. C., and Li, Z. J. (2018). Enhanced photocatalytic $CO_2$ reduction activity of Z-scheme CdS/$BiVO_4$ nanocomposite with thinner $BiVO_4$ nanosheets. *J. $Co_2$ Util.* 28, 15–25. doi:10.1016/j.jcou.2018.09.008

White, J. L., Baruch, M. F., Pander, J. E., Hu, Y., Fortmeyer, I. C., Park, J. E., et al. (2015). Light-driven heterogeneous reduction of carbon dioxide: photocatalysts and photoelectrodes. *Chem. Rev.* 115 (23), 12888–12935. doi:10.1021/acs.chemrev.5b00370

Woo, S. J., Choi, S., Kim, S. Y., Kim, P. S., Jo, J. H., Kim, C. H., et al. (2019). Highly selective and durable photochemical $CO_2$ reduction by molecular Mn(I) catalyst fixed on particular dye-sensitized $TiO_2$ platform. *ACS Catal.* 9 (3), 2580–2593. doi:10.1021/acscatal.8b03816

Wu, J., Li, X., Shi, W., Ling, P., Sun, Y., Jiao, X., et al. (2018). Efficient visible-light-driven $CO_2$ reduction mediated by defect-engineered BiOBr atomic layers. *Angew. Chem. Int. Ed.* 130 (28), 8855–8859. doi:10.1002/ange.201803514

Wu, J., Feng, Y., Logan, B. E., Dai, C., Han, X., Li, D., et al. (2019). Preparation of Al–O-Linked porous-g-$C_3N_4$/$TiO_2$-nanotube Z-scheme composites for efficient photocatalytic $CO_2$ conversion and 2,4-dichlorophenol decomposition and mechanism. *ACS Sustain. Chem. Eng.* 7, 15289–15296. doi:10.1021/acssuschemeng.9b02489

Xia, X. H., Jia, Z. J., Yu, Y., Liang, Y., Wang, Z., and Ma, L. L. (2007). Preparation of multi-walled carbon nanotube supported $TiO_2$ and its photocatalytic activity in the reduction of $CO_2$ with $H_2O$. *Carbon* 45 (4), 717–721. doi:10.1016/j.carbon.2006.11.028

Xie, S., Wang, Y., Zhang, Q., Fan, W., Deng, W., and Wang, Y. (2013). Photocatalytic reduction of $CO_2$ with $H_2O$: significant enhancement of the activity of Pt-$TiO_2$ in $CH_4$ formation by addition of MgO. *Chem. Commun.* 49 (24), 2451–2453. doi:10.1039/c3cc00107e

Xie, S., Wang, Y., Zhang, Q., Deng, W., and Wang, Y. (2014). MgO-and Pt-promoted $TiO_2$ as an efficient photocatalyst for the preferential reduction of carbon dioxide in the presence of water. *ACS Catal.* 4, 3644–3653. doi:10.1021/cs500648p

Xie, S., Zhang, Q., Liu, G., and Wang, Y. (2016). Photocatalytic and photoelectrocatalytic reduction of $CO_2$ using heterogeneous catalysts with controlled nanostructures. *Chem. Commun.* 52 (1), 35–59. doi:10.1039/c5cc07613g

Xiong, Z., Wang, H., Xu, N., Li, H., Fang, B., Zhao, Y., et al. (2015). Photocatalytic reduction of $CO_2$ on $Pt^{2+}$-$Pt^0$/$TiO_2$ nanoparticles under UV/Vis light irradiation: a combination of $Pt^{2+}$ doping and Pt nanoparticles deposition. *Inter. J. Hydrogen Energ.* 40 (32), 10049–10062. doi:10.1016/j.ijhydene.2015.06.075

Xiong, Z., Luo, Y., Zhao, Y., Zhang, J., Zheng, C., and Wu, J. C. S. (2016). Synthesis, characterization and enhanced photocatalytic $CO_2$ reduction activity of graphene supported $TiO_2$ nanocrystals with coexposed {001} and {101} facets. *Phys. Chem. Chem. Phys.* 18 (19), 13186–13195. doi:10.1039/c5cp07854g

Xiong, Z., Lei, Z., Chen, X., Gong, B., Zhao, Y., Zhang, J., et al. (2017a). $CO_2$ photocatalytic reduction over Pt deposited $TiO_2$ nanocrystals with coexposed {101} and {001} facets: effect of deposition method and Pt precursors. *Catal. Commu.* 96, 1–5. doi:10.1016/j.catcom.2017.03.013

Xiong, Z., Lei, Z., Gong, B., Chen, X., Zhao, Y., Zhang, J., et al. (2017b). A novel reaction mode using $H_2$ produced from solid-liquid reaction to promote $CO_2$ reduction through solid-gas reaction. *Catal. Commun.* 89, 4–8. doi:10.1016/j.catcom.2016.10.010

Xiong, Z., Lei, Z., Kuang, C. C., Chen, X., Gong, B., Zhao, Y., et al. (2017c). Selective photocatalytic reduction of $CO_2$ into $CH_4$ over Pt-$Cu_2O$ $TiO_2$ nanocrystals: the interaction between Pt and $Cu_2O$ cocatalysts. *Appl. Catal. B* 202, 695–703. doi:10.1016/j.apcatb.2016.10.001

Xiong, Z., Lei, Z., Li, Y., Dong, L., Zhao, Y., and Zhang, J. (2018). A review on modification of facet-engineered $TiO_2$ for photocatalytic $CO_2$ reduction. *J. Photochem. Photobiol. C* 36, 24–47. doi:10.1016/j.jphotochemrev.2018.07.002

Xiong, J., Zhang, M., and Cheng, G. (2020). Facile polyol-triggered anatase-rutile heterophase $TiO_{2-x}$ nanoparticles for enhancing photocatalytic $CO_2$ reduction. *J. Colloid Interf. Sci.* 579, 872–877. doi:10.1016/j.jcis.2020.06.103

Xu, Q., Yu, J., Zhang, J., Zhang, J., and Liu, G. (2015). Cubic anatase $TiO_2$ nanocrystals with enhanced photocatalytic $CO_2$ reduction activity. *Chem. Commun.* 51 (37), 7950–7953. doi:10.1039/c5cc01087j

Xu, F., Meng, K., Cheng, B., Yu, J., and Ho, W. (2018a). Enhanced photocatalytic activity and selectivity for $CO_2$ reduction over a $TiO_2$ nanofibre mat using Ag and MgO as bi-cocatalyst. *ChemCatChem* 11, 465–472. doi:10.1002/cctc.201801282

Xu, F., Zhang, J., Zhu, B., Yu, J., and Xu, J. (2018b). $CuInS_2$ sensitized $TiO_2$ hybrid nanofibers for improved photocatalytic $CO_2$ reduction. *Appl. Catal. B* 230, 194–202. doi:10.1016/j.apcatb.2018.02.042

Xu, S., and Carter, E. A. (2019). Theoretical insights into heterogeneous (photo) electrochemical $CO_2$ reduction. *Chem. Rev.* 119, 6631–6669. doi:10.1021/acs.chemrev.8b00481

Yang, G., Chen, D., Ding, H., Feng, J., Zhang, J. Z., Zhu, Y., et al. (2017). Well-designed 3D $ZnIn_2S_4$ nanosheets/$TiO_2$ nanobelts as direct Z-scheme photocatalysts for $CO_2$ photoreduction into renewable hydrocarbon fuel with high efficiency. *Appl. Catal. B* 219, 611–618. doi:10.1016/j.apcatb.2017.08.016

Ye, L., Jin, X., Liu, C., Ding, C., Xie, H., Chu, K. H., et al. (2016). Thickness-ultrathin and bismuth-rich strategies for BiOBr to enhance photoreduction of $CO_2$ into solar fuels. *Appl. Catal. B* 187, 281–290. doi:10.1016/j.apcatb.2016.01.044

You, F., Wan, J., Qi, J., Mao, D., Yang, N., Zhang, Q., et al. (2020). Lattice distortion in hollow multi-shelled structures for efficient visible light $CO_2$ reduction with

$SnS_2/SnO_2$ junction. *Angew. Chem. Int. Ed.* 132 (2), 731–734. doi:10.1002/ange.201912069

Yu, J., Low, J., Xiao, W., Zhou, P., and Jaroniec, M. (2014). Enhanced photocatalytic $CO_2$-reduction activity of anatase $TiO_2$ by coexposed {001} and {101} facets. *J. Am. Chem. Soc.* 136 (25), 8839–8842. doi:10.1021/ja5044787

Yu, B., Zhou, Y., Li, P., Tu, W., Li, P., Tang, L., et al. (2016). Photocatalytic reduction of $CO_2$ over $Ag/TiO_2$ nanocomposites prepared with a simple and rapid silver mirror method. *Nanoscale* 8 (23), 11870–11874. doi:10.1039/c6nr02547a

Zeng, G., Qiu, J., Li, Z., Pavaskar, P., and Cronin, S. B. (2014). $CO_2$ reduction to methanol on $TiO_2$-passivated GaP photocatalysts. *ACS Cataly* 4 (10), 3512–3516. doi:10.1021/cs500697w

Zeng, S., Vahidzadeh, E., VanEssen, C. G., Kar, P., Kisslinger, R., Goswami, A., et al. (2020). Optical control of selectivity of high rate $CO_2$ photoreduction *via* interband- or hot electron Z-scheme reaction pathways in Au-$TiO_2$ plasmonic photonic crystal photocatalyst. *Appl. Catal. B* 267, 118644. doi:10.1016/j.apcatb.2020.118644

Zhang, B., and Sun, L. (2019). Artificial photosynthesis: opportunities and challenges of molecular catalysts. *Chem. Soc. Rev.* 48, 2216–2264. doi:10.1039/c8cs00897c

Zhang, J., Fu, J., Chen, S., Lv, J., and Dai, K. (2018). 1D carbon nanofibers@$TiO_2$ core-shell nanocomposites with enhanced photocatalytic activity toward $CO_2$ reduction. *J. Alloys Compd.* 746, 168–176. doi:10.1016/j.jallcom.2018.02.265

Zhang, L., Cao, H., Pen, Q., Wu, L., Hou, G., Tang, Y., et al. (2018). Embedded CuO nanoparticles@$TiO_2$-nanotube arrays for photoelectrocatalytic reduction of $CO_2$ to methanol. *Electrochim. Acta* 283, 1507–1513. doi:10.1016/j.electacta.2018.07.072

Zhang, L., and Jaroniec, M. (2018). Toward designing semiconductor-semiconductor heterojunctions for photocatalytic applications. *Appl. Surf. Sci.* 430, 2–17. doi:10.1016/j.apsusc.2017.07.192

Zhang, L., Cao, H., Lu, Y., Zhang, H., Hou, G., Tang, Y., et al. (2020). Effective combination of $CuFeO_2$ with high temperature resistant Nb-doped $TiO_2$ nanotube arrays for $CO_2$ photoelectric reduction. *J. Colloid Interf. Sci.* 568, 198–206. doi:10.1016/j.jcis.2020.01.082

Zhao, H., Zheng, X., Feng, X., and Li, Y. (2018). $CO_2$ reduction by plasmonic Au nanoparticle-decorated $TiO_2$ photocatalyst with an ultrathin $Al_2O_3$ interlayer. *J. Phys. Chem. C* 122, 18949–18956. doi:10.1021/acs.jpcc.8b04239

Zhao, Y., Wei, Y., Wu, X., Zheng, H., Zhao, Z., Liu, J., et al. (2018). Graphene-wrapped $Pt/TiO_2$ photocatalysts with enhanced photogenerated charges separation and reactant adsorption for high selective photoreduction of $CO_2$ to $CH_4$. *Appl. Catal. B* 226, 360–372. doi:10.1016/j.apcatb.2017.12.071

Zhu, S., Liao, W., Zhang, M., and Liang, S. (2019). Design of spatially separated Au and CoO Ziaratidual cocatalysts on hollow $TiO_2$ for enhanced photocatalytic activity towards the reduction of $CO_2$ to $CH_4$. *Chem. Eng. J.* 361, 461–469. doi:10.1016/j.cej.2018.12.095

Ziarati, A., Badiei, A., Luque, R., Dadras, M., and Burgi, T. (2020). Visible light $CO_2$ reduction to $CH_4$ using hierarchical yolk@shell $TiO_{2-x}H_x$ modified with plasmonic Au-Pd nanoparticles. *ACS Sustain. Chem. Eng.* 8, 3689–3696. doi:10.1021/acssuschemeng.9b06751

Zubair, M., Kim, H., Razzaq, A., Grimes, C. A., and In, S. I. (2018). Solar spectrum photocatalytic conversion of $CO_2$ to $CH_4$ utilizing $TiO_2$ nanotube arrays embedded with graphene quantum dots. *J. $Co_2$ Util.* 26, 70–79. doi:10.1016/j.jcou.2018.04.004

**Conflict of Interest:** The authors declare that the research was conducted in the absence of any commercial or financial relationships that could be construed as a potential conflict of interest.